
MULTIFIDELITY DEEP OPERATOR NETWORKS

Amanda A. Howard

Pacific Northwest National Laboratory
Richland, WA

Mauro Perego

Center for Computing Research
Sandia National Laboratories
Albuquerque, NM

George E. Karniadakis

Division of Applied Mathematics
Brown University, Providence, RI
Pacific Northwest National Laboratory, Richland, WA

Panos Stinis

Pacific Northwest National Laboratory
Richland, WA
panagiotis.stinis@pnnl.gov

April 21, 2022

ABSTRACT

Operator learning for complex nonlinear operators is increasingly common in modeling physical systems. However, training machine learning methods to learn such operators requires a large amount of expensive, high-fidelity data. In this work, we present a composite Deep Operator Network (DeepONet) for learning using two datasets with different levels of fidelity, to accurately learn complex operators when sufficient high-fidelity data is not available. Additionally, we demonstrate that the presence of low-fidelity data can improve the predictions of physics-informed learning with DeepONets.

Keywords: multifidelity, physics-informed machine learning, deep learning, computational physics

In many applications across science and engineering it is common to have access to disparate types of data with different levels of fidelity. In general, low-fidelity data is easier to obtain in greater quantities, but it may be too inaccurate or not dense enough to accurately train a machine learning model. High-fidelity data is costly to obtain, so there may not be sufficient data to use in training, however, it is more accurate. A small amount of high fidelity data, such as from measurements, combined with low fidelity data, can improve predictions when used together [1]. In this work we consider the motivating example of a low-order numerical model that is less computationally expensive, so it can be used to generate large amounts of low-fidelity data. However, low-order numerical models are less accurate and a trained machine learning model will only be as accurate as the model. In contrast, a higher-order numerical model can be too costly to run, or experimental data can be too expensive to generate in sufficient quantities for training. This situation is exacerbated when the machine learning model is required to approximate not just a function, but an operator, *e.g.* the evolution operator of a partial differential equation. In the current work, we present a method that can combine low-fidelity and high-fidelity data to produce more accurate operator approximations than using either dataset alone. In addition, the proposed approach allows the incorporation of information from physics to further improve the approximation accuracy.

The Deep Operator Network (DeepONet) framework [27], inspired by the universal approximation theorem for operators [7, 2], allows for learning of operators between infinite-dimensional spaces. DeepONets have been accurately applied to a wide range of applications [41, 38, 16], including bubble dynamics across a range of length scales [24], prediction of failure due to cracks [16], and prediction of linear instability waves in high-speed boundary layers [12]. More recently, [46] introduced the modified DeepONet architecture, which provides more accurate results across a range of problems.

Physics-informed neural networks usually train for one set of input parameters [37, 42, 22, 44, 36, 23]. By construction, DeepONets are suited for training for a whole range of input parameters. In addition, because DeepONet outputs are differentiable with respect to the input coordinates, the same framework used in physics-informed neural networks (PINNs) [37], which relies on automatic differentiation [17, 3], can also be applied to DeepONets. Indeed, the work in [47] and [45] extends the DeepONet framework by allowing the inclusion of physics-informed terms in the loss

function. This can potentially eliminate the need for training data in the form of input-output pairs required to find *e.g.*, the solution to partial differential equations (PDEs).

Previous work with PINNs has enabled multifidelity learning of functions with both data and physics-informed training [31, 21, 39]. This work can broadly be split into three categories: transfer learning, where the network is first trained for the low-fidelity data, then a correction is found to correct the low-fidelity output, simultaneous training, and consecutive training. Transfer learning can be trained with or without physics [43, 11, 9]. The approaches in [5] and [19] use transfer learning and a two-step training process to first enforce (approximate) physics, and then use a small amount of high-fidelity data to correct the trained PINN output. This process applies when the physics is either not known exactly or the cost to generate low-fidelity data with a solver is too high. In simultaneous training, [28] learns both the linear and nonlinear correlations between the low-fidelity and high-fidelity data, by simultaneously training the low- and high-fidelity networks. This method allows for problems with complex correlations between the two datasets [29]. Simultaneous training can also be applied successfully without physics [28, 48]. In the consecutive training category, [25] trains three networks, two low- and high-fidelity physics-constrained neural networks and a third neural network to learn the correlation between the low- and high-fidelity output. We note that very recent work considers bifidelity data with DeepONets, however, the authors do not consider physics-informed losses, and learn only a linear correlation between the low- and high-fidelity data [10].

In the current work, we consider the case where we have a large amount of low-fidelity data and either a smaller amount of higher quality high-fidelity data or knowledge of the physical laws the system obeys. We learn both the linear and nonlinear correlation between the high- and low-fidelity data, which allows to learn complex correlations between the data sets. The low-fidelity and high-fidelity datasets do not need to be for the same set of input functions, giving additional flexibility to this method. We note that the framework presented here is adaptable, and that the physical laws can instead be applied on the low-fidelity network, with corrections from high-fidelity data. Additionally, the framework can enforce both data and physics within a single level of fidelity. For example, if one has a low-order numerical solver that approximates a PDE and sparse measurements of the true system, both the measurements and the PDE can be enforced at the high-fidelity level and the low-order numerical data can be enforced at the low-fidelity level.

The paper is organized as follows. We introduce the architecture and notation in Section 1. We divide multifidelity DeepONets into data-driven and physics-informed. In Section 2, we consider illustrative one- and two-dimensional data-driven examples. As a motivating application to a complex problem, we apply in Section 2.5 the data-driven multifidelity DeepONet framework with low- and high-fidelity simulations for ice sheet dynamics. In Section 3, we investigate the performance of the physics-informed multifidelity DeepONet framework for the case of enforcing physics in the absence of high-fidelity data. In end the paper in Section 4 with a brief discussion and suggestions for future work.

1 Multifidelity DeepONets

1.1 Architecture

A “standard” unstacked single fidelity DeepONet consists of two neural networks, the branch and the trunk, which are trained simultaneously [27]. The input to the branch network is a function \mathbf{u} discretized at points $\{x_i\}_{i=1}^M$, and the output is $[b_1, b_2, \dots, b_p]^T \in \mathbb{R}^Q$. The input to the trunk net is the coordinates $\mathbf{x} \in \mathbb{R}^n$, and the trunk output is $[t_1, t_2, \dots, t_p]^T \in \mathbb{R}^Q$. The DeepONet output can be expressed as

$$\mathcal{G}_{SF}^\theta(\mathbf{u})(\mathbf{x}) = \sum_{k=1}^p b_k t_k \quad (1)$$

where θ denotes the trainable parameters of the unstacked single fidelity DeepONet (for a detailed description see [26, 27]).

In this work we use “modified” DeepONets, proposed in [46]. Modified DeepONets include the addition of two encoder networks, one each for the branch and trunk networks, which are included in each hidden layer of the branch and trunk networks through a convex combination. The modified DeepONet has been shown to improve performance of the method [46]. Following the notation in [46], we denote the branch encoder by \mathbf{U} with weights \mathbf{W}_u and biases \mathbf{b}_u and denote the trunk encoder by \mathbf{V} with weights \mathbf{W}_x and biases \mathbf{b}_x . Thus, $\mathbf{U} = \phi(\mathbf{W}_u \mathbf{u} + \mathbf{b}_u)$ and $\mathbf{V} = \phi(\mathbf{W}_x \mathbf{x} + \mathbf{b}_x)$, where ϕ is an activation function. We consider a modified DeepONet with L layers and denote the weights and biases of the branch and trunk networks by $\left\{ \mathbf{W}_u^{(l)}, \mathbf{b}_u^{(l)} \right\}_{l=1}^L$ and $\left\{ \mathbf{W}_x^{(l)}, \mathbf{b}_x^{(l)} \right\}_{l=1}^L$, respectively. Then, the forward pass of

the modified DeepONet is given by:

$$\mathbf{Z}_u^{(1)} = \phi \left(\mathbf{W}_u^{(1)} \mathbf{u} + \mathbf{b}_u^{(1)} \right), \quad \mathbf{Z}_x^{(1)} = \phi \left(\mathbf{W}_x^{(1)} \mathbf{x} + \mathbf{b}_x^{(1)} \right) \quad (2)$$

$$\mathbf{H}_u^{(l)} = (1 - \mathbf{Z}_u^{(l)}) \odot \mathbf{U} + \mathbf{Z}_u^{(l)} \odot \mathbf{V}, \quad \mathbf{H}_x^{(l)} = (1 - \mathbf{Z}_x^{(l)}) \odot \mathbf{U} + \mathbf{Z}_x^{(l)} \odot \mathbf{V}, \quad l = 1, \dots, L-1 \quad (3)$$

$$\mathbf{Z}_u^{(l)} = \phi \left(\mathbf{W}_u^{(l)} \mathbf{H}_u^{(l-1)} + \mathbf{b}_u^{(l)} \right), \quad \mathbf{Z}_x^{(l)} = \phi \left(\mathbf{W}_x^{(l)} \mathbf{H}_x^{(l-1)} + \mathbf{b}_x^{(l)} \right), \quad l = 2, \dots, L-1 \quad (4)$$

$$\mathbf{H}_u^{(L)} = \mathbf{W}_u^{(L)} \mathbf{H}_u^{(L-1)} + \mathbf{b}_u^{(L)}, \quad \mathbf{H}_x^{(L)} = \mathbf{W}_x^{(L)} \mathbf{H}_x^{(L-1)} + \mathbf{b}_x^{(L)} \quad (5)$$

$$G^\theta(\mathbf{u})(\mathbf{y}) = \langle \mathbf{H}_u^{(L)}, \mathbf{H}_x^{(L)} \rangle \quad (6)$$

Here, \odot represents point-wise multiplication and $\langle \cdot, \cdot \rangle$ represents an inner product. Note that for single fidelity DeepONets no activation function is applied to the last layer.

The multifidelity DeepONet framework consists of three blocks, trained simultaneously. A schematic of the multifidelity DeepONet architecture is given in Fig. 1 for both data-driven and physics-informed cases. The low-fidelity block is a standard modified DeepONet [46]. It represents an approximation of the low-fidelity data. The nonlinear block encodes the nonlinear correlation between the output of the low-fidelity network and the high-fidelity data or physics. The nonlinear block is a modified DeepONet with the activation function applied on every layer. The linear block is a standard DeepONet with no activation functions and is used to approximate the linear correlation between the output of the low-fidelity block and the high-fidelity data or physics. We note that the outputs of the linear and nonlinear DeepONets are continuously differentiable with respect to their input coordinates, and therefore we can use automatic differentiation on the outputs [17, 3]. If a low-fidelity solver is available, the solver can be used in place of the low-fidelity block. A discussion of this case is given in Appendix C.

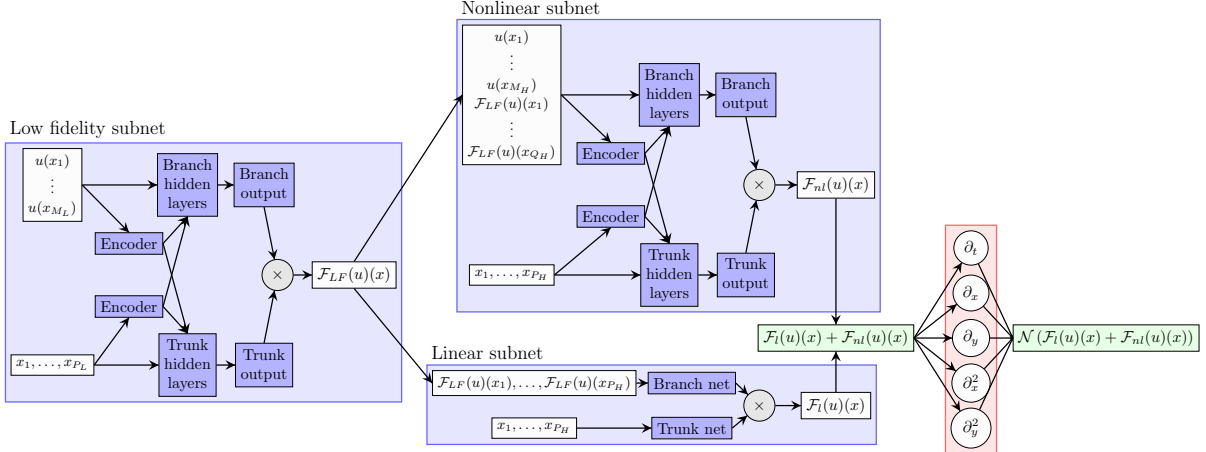


Figure 1: Schematic of the composite physics-informed multifidelity DeepONet setup. $\mathcal{F}_{LF}(u)(x)$, $\mathcal{F}_{nl}(u)(x)$, and $\mathcal{F}_l(u)(x)$ are the outputs of the low-fidelity, nonlinear, and linear DeepONet subnets.

1.2 Notation

Consider a nonlinear operator G mapping from one space of functions to another space of functions, $G : \mathcal{U} \rightarrow \mathcal{S}$. It has been shown that a neural network with a single hidden layer can accurately approximate the operator G [6, 7, 27]. Denote the input function to the operator by $u \in \mathcal{U}$, and denote the output function by $G(u) \in \mathcal{S}$. For any point x in the domain our network takes input (u, x) and outputs $G(u)(x)$.

Now, following the notation in [46], we consider a linear or nonlinear differential operator $\mathcal{N} : \mathcal{U} \times \mathcal{S} \rightarrow \mathcal{V}$, where $(\mathcal{U}, \mathcal{S}, \mathcal{V})$ is a triplet of Banach spaces, and a general parametric PDE of the form $\mathcal{N}(u, s) = 0$ with boundary conditions $\mathcal{B}(u, s) = 0$. Here, $u \in \mathcal{U}$ is the input function, and $s \in \mathcal{S}$ is a function satisfying the differential operator subject to the boundary conditions. \mathcal{B} can represent Dirichlet, Neumann, Robin, or periodic boundary conditions. With this notation, if for all $u \in \mathcal{U}$ there exists a unique solution $s = s(u)$ to $\mathcal{N}(u, s) = 0$ and $\mathcal{B}(u, s) = 0$, the solution can be represented as an operator $G : \mathcal{U} \rightarrow \mathcal{S}$, where $G(u) = s(u)$ [46].

A schematic of the multifidelity DeepONet architecture is given in Fig. 1 for both data-driven and physics-informed cases. In both cases, we train three DeepONets simultaneously. The low-fidelity subnet approximates the low-fidelity

operator. We assume that we have low-fidelity data with inputs to the operators given by $\mathbf{u}^j \in \mathcal{U}$ for $j = 1, \dots, N_L$. While each \mathbf{u}^j can be a continuous function, we need to discretize \mathbf{u}^j and therefore evaluate \mathbf{u}^j on a set of values called sensors for input to the low-fidelity branch net, given by $(\mathbf{u}^j(x_1), \dots, \mathbf{u}^j(x_{M_L}))$. The output values are given by $(y_L(\mathbf{u}^j)(x_1), \dots, y_L(\mathbf{u}^j)(x_{P_L}))_{j=1, \dots, N_L} \in \mathcal{S}$. We denote the output of the low-fidelity, nonlinear, and linear subnets by $\mathcal{F}_{LF}(\mathbf{u})(x)$, $\mathcal{F}_{nl}(\mathbf{u})(x)$, and $\mathcal{F}_l(\mathbf{u})(x)$, respectively. The nonlinear and linear subnets take the output of the low-fidelity subnet as part or all of their branch networks, and the sum of the linear and nonlinear subnet outputs approximates the high-fidelity operator. The input to the linear branch net is given by $[\mathcal{F}_{LF}^\theta(\mathbf{u})(\mathbf{x}_1), \dots, \mathcal{F}_{LF}^\theta(\mathbf{u})(\mathbf{x}_{P_H})]$, that is, the input is the low-fidelity network evaluated at all points used in the input to the linear trunk net. The input to the nonlinear branch net is given by $[\mathbf{u}(\mathbf{x}_1), \dots, \mathbf{u}(\mathbf{x}_{M_H}), \mathcal{F}_{LF}^\theta(\mathbf{u})(\mathbf{x}_1), \dots, \mathcal{F}_{LF}^\theta(\mathbf{u})(\mathbf{x}_{Q_H})]^T$. In this way, the nonlinear subnet learns the nonlinear correlation between the low- and high-fidelity operators, and the linear subnet learns the linear correlation between the low- and high-fidelity operators. Typically, we take $Q_H = P_L$ and augment the nonlinear branch net input with the output of the low-fidelity network at all low-fidelity training points, however, in some cases choosing a different set of output points can improve performance by reducing the number of points needed in the evaluation and therefore increasing speed, or by highlighting important features. We denote by $\theta = (\theta_{nl}, \theta_l, \theta_{LF})$ the set of all trainable parameters of the three subnetworks.

The low-fidelity loss for a given input function \mathbf{u}^j is given by

$$\mathcal{L}_{LF}(\mathbf{u}^j, \theta_{LF}) = \frac{1}{P_L} \sum_{k=1}^{P_L} |y_L(\mathbf{u}^j)(x_k) - \mathcal{F}_{LF}^\theta(\mathbf{u}^j)(x_k)|^2 \quad (7)$$

and the full low-fidelity loss is then

$$\mathcal{L}_{LF}(\theta_{LF}) = \frac{1}{N_L} \sum_{j=1}^{N_L} \mathcal{L}_{LF}(\mathbf{u}^j, \theta_{LF}) = \frac{1}{N_L P_L} \sum_{j=1}^{N_L} \sum_{k=1}^{P_L} |y_L(\mathbf{u}^j)(x_k) - \mathcal{F}_{LF}^\theta(\mathbf{u}^j)(x_k)|^2. \quad (8)$$

For the high-fidelity networks we divide into two cases depending on whether high-fidelity data or physical knowledge of the system is enforced.

1.2.1 Data-driven multifidelity notation

In the data-driven case, we assume we have high-fidelity data with input values to the operator $\mathbf{u}^k \in \mathcal{U}$ for $k = 1, \dots, N_H$ evaluated on sensors $(\mathbf{u}^k(x_1), \dots, \mathbf{u}^k(x_{M_H}))$. We note that we do not need the high-fidelity input values to be the same as the low-fidelity values, that is $\{\mathbf{u}^k\}_{k=1}^{N_H}$ and $\{\mathbf{u}^j\}_{j=1}^{N_L}$ can be independent sets. The output values are given by $(y_H(\mathbf{u}^k)(x_1), \dots, y_H(\mathbf{u}^k)(x_{P_H})) \in \mathcal{S}$. We simultaneously train three DeepONets to learn the low-fidelity operator and the linear and nonlinear correlations between the low-fidelity operator and the high-fidelity operator. The full high-fidelity loss is

$$\mathcal{L}_{HF}(\theta_{nl}, \theta_l) = \frac{1}{N_H P_H} \sum_{j=1}^{N_H} \sum_{k=1}^{P_H} |y_H(\mathbf{u}^j)(x_k) - \mathcal{F}_{nl}^\theta(\mathbf{u}^j)(x_k) - \mathcal{F}_l^\theta(\mathbf{u}^j)(x_k)|^2. \quad (9)$$

The full data-driven loss is then given by:

$$\mathcal{L}_{DD}(\theta) = \lambda_1 \mathcal{L}_{HF}(\theta_{nl}, \theta_l) + \lambda_2 \mathcal{L}_{LF}(\theta_{LF}) + \lambda_3 \left(\sum w_{nl}^2 + \sum b_{nl}^2 \right) + \lambda_4 \left(\sum w_{LF}^2 + \sum b_{LF}^2 \right). \quad (10)$$

Here, w_{nl} and b_{nl} are the weights and biases from the nonlinear branch net and w_{LF} and b_{LF} are the weights and biases from the low-fidelity branch net. The regularization term on the nonlinear branch net serves to minimize the nonlinear correlation, forcing the network to learn a linear correlation if appropriate. The regularization term on the low-fidelity branch net prevents over-fitting of the low-fidelity data. λ_i , $i = 1, 2, 3, 4$ are weights that can be chosen for each case.

We compare our results with a single fidelity modified DeepONet trained on the high-fidelity data. The full single fidelity data-driven loss is

$$\mathcal{L}_{SF}(\theta_{SF}) = \frac{1}{N_H P_H} \sum_{j=1}^{N_H} \sum_{k=1}^{P_H} |y_H(\mathbf{u}^j)(x_k) - \mathcal{G}_{SF}^\theta(\mathbf{u}^j)(x_k)|^2, \quad (11)$$

where $\mathcal{G}_{SF}^\theta(\mathbf{u}^j)(x_k)$ denotes the output from the single fidelity modified DeepONet with parameters θ_{SF} .

1.2.2 Physics-informed multifidelity notation

In the second case, we assume we have no high-fidelity training data in the form of input-output pairs for the high-fidelity network, but that the output does satisfy a PDE with appropriate boundary conditions. The boundary condition loss for a given input function $\{\mathbf{u}^i\}_{i=1}^{N_H}$ can be written as:

$$\mathcal{L}_B(\mathbf{u}^i, \theta_{nl}, \theta_l) = \frac{1}{P_{BC}} \sum_{j=1}^{P_{BC}} |\mathcal{B}(\mathbf{u}^i, \mathcal{F}_{nl}^\theta(\mathbf{u}^i)(\mathbf{x}_j) + \mathcal{F}_l^\theta(\mathbf{u}^i)(\mathbf{x}_j))| \quad (12)$$

where the points $\{\mathbf{x}_j\}_{j=1}^{P_{BC}}$ are randomly chosen on the boundary of the domain. The full boundary condition loss is then:

$$\mathcal{L}_B(\theta_{nl}, \theta_l) = \frac{1}{N_H P_{BC}} \sum_{i=1}^{N_H} \sum_{j=1}^{P_{BC}} |\mathcal{B}(\mathbf{u}^i, \mathcal{F}_{nl}^\theta(\mathbf{u}^i)(\mathbf{x}_j) + \mathcal{F}_l^\theta(\mathbf{u}^i)(\mathbf{x}_j))|. \quad (13)$$

We treat initial conditions as a special case of boundary conditions.

We also consider the loss in satisfying the parametric PDE, given by:

$$\mathcal{L}_{physics}(\theta_{nl}, \theta_l) = \frac{1}{N_H P_p} \sum_{i=1}^{N_H} \sum_{j=1}^{P_p} |\mathcal{N}(\mathbf{u}^i, \mathcal{F}_{nl}^\theta(\mathbf{u}^i)(\mathbf{x}_j) + \mathcal{F}_l^\theta(\mathbf{u}^i)(\mathbf{x}_j))|, \quad (14)$$

where the points $\{\mathbf{x}_j\}_{j=1}^{P_p}$ are randomly chosen on the interior of the domain.

For ease of notation, we split the boundary condition operator in two parts, the part representing the initial conditions (\mathcal{L}_{BC}) and the part representing the initial condition (\mathcal{L}_{IC}). Then, the full multifidelity physics-informed loss can be written as:

$$\begin{aligned} \mathcal{L}_{PI}(\theta) = & \lambda_1 \mathcal{L}_{physics}(\theta_{nl}, \theta_l) + \lambda_2 \mathcal{L}_{LF}(\theta_{LF}) + \lambda_5 \mathcal{L}_{IC}(\theta_{nl}, \theta_l) + \lambda_6 \mathcal{L}_{BC}(\theta_{nl}, \theta_l) \\ & + \lambda_3 \left(\sum w_{nl}^2 + \sum b_{nl}^2 \right) + \lambda_4 \left(\sum w_{LF}^2 + \sum b_{LF}^2 \right). \end{aligned} \quad (15)$$

We compare our results with a single fidelity physics-informed DeepONet. The full single fidelity physics-informed loss is

$$\mathcal{L}_{PI}(\theta) = \lambda_1 \mathcal{L}_{physics}(\theta) + \lambda_5 \mathcal{L}_{IC}(\theta) + \lambda_6 \mathcal{L}_{BC}(\theta). \quad (16)$$

While we consider only the case where physics is applied as a high-fidelity correction to low-fidelity data, it is also possible to consider a case where physics represents a low-fidelity model, such as when the exact physics of the system are not known. In that case, the low-fidelity physics-informed DeepONet could use high-fidelity data from, *e.g.* experiments, together as a training set.

2 Data-driven multifidelity DeepONets

2.1 One-dimensional, jump function

We first consider a case where the low- and high-fidelity data are represented by jump functions with a linear correlation. We show that we can recover both the jump and the linear correlation accurately. The low- and high-fidelity data are given by:

$$y_L(u)(x) = \begin{cases} 0.5(6x - 2)^2 \sin(u) + 10(x - 0.5) - 5 & x \leq 0.5 \\ 0.5(6x - 2)^2 \sin(u) + 10(x - 0.5) - 2 & x > 0.5 \end{cases} \quad (17)$$

$$y_H(u)(x) = 2y_L(u)(x) - 20x + 20 \quad (18)$$

$$u = ax - 4 \quad (19)$$

for $x \in [0, 1]$ and $a \in [10, 14]$. Parameters are given in Tab. 3 (see Appendix B.1) and results in Fig. 2. The learned linear correlation is:

$$\mathcal{F}_l(u)(x) = 1.9479\mathcal{F}_{LF}(u)(x) - 19.1719x + 19.3459 - 0.04870x\mathcal{F}_{LF}(u)(x). \quad (20)$$

The learned linear correlation accurately captures the exact correlation. Fig. 2c shows that the single fidelity method fails to capture the jump, with a large error at $x = 0.5$, and the absolute error is quite large across the domain. With the multifidelity method, both the high-fidelity and low-fidelity errors are smaller. The errors are concentrated at the jump due to the limitations of the resolution of the low-fidelity training set.

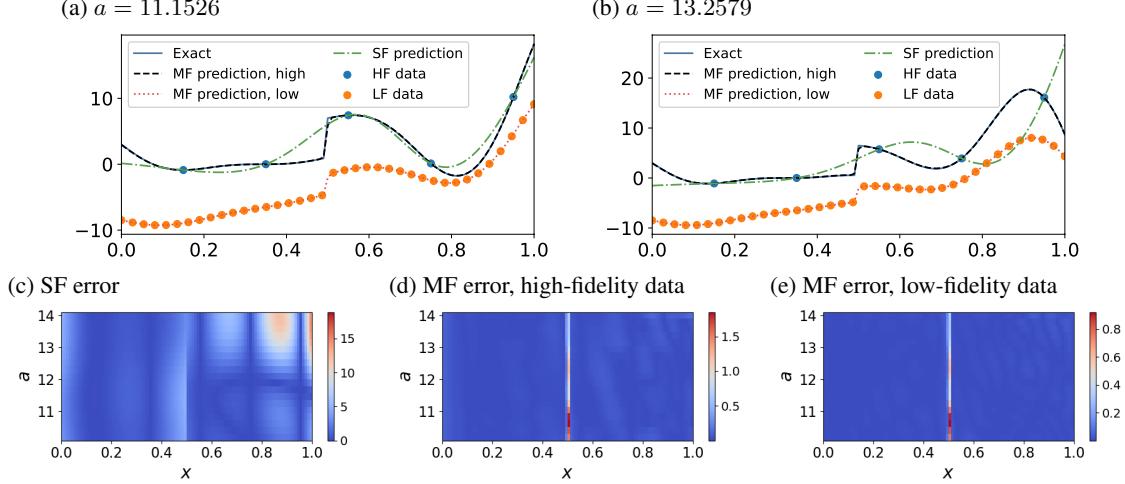


Figure 2: Data-driven multifidelity: one-dimensional, jump function. (a-b) Results of the single fidelity and multifidelity predictions of the high- and low-fidelity data. (c) Single-fidelity error as a function of a and x , (d) multifidelity high-fidelity prediction error as a function of a and x , and (e) multifidelity low-fidelity prediction error as a function of a and x .

2.2 One-dimensional, correlation with u

The multifidelity data-driven training is able to capture complex, nonlinear correlations between the low- and high-fidelity datasets. To illustrate this, we consider a case where the correlation depends on the input function, u :

$$y_L(u)(x) = \sin(u) + x - 0.25u \quad (21)$$

$$y_H(u)(x) = \sin(u) \quad (22)$$

$$u = ax - 4 \quad (23)$$

for $x \in [0, 1]$ and $a \in [10, 14]$. We have $y_H(u)(x) = y_L(u)(x) - x + 0.25u = y_L(u)(x) - x + 0.25(ax - 4)$. Parameters are given in Tab. 4 (see Appendix B.2) and results in Fig. 3. The single fidelity case has large errors across the (x, a) domain. The error in the high-fidelity output from the multifidelity training is concentrated where the low-fidelity error is the highest.

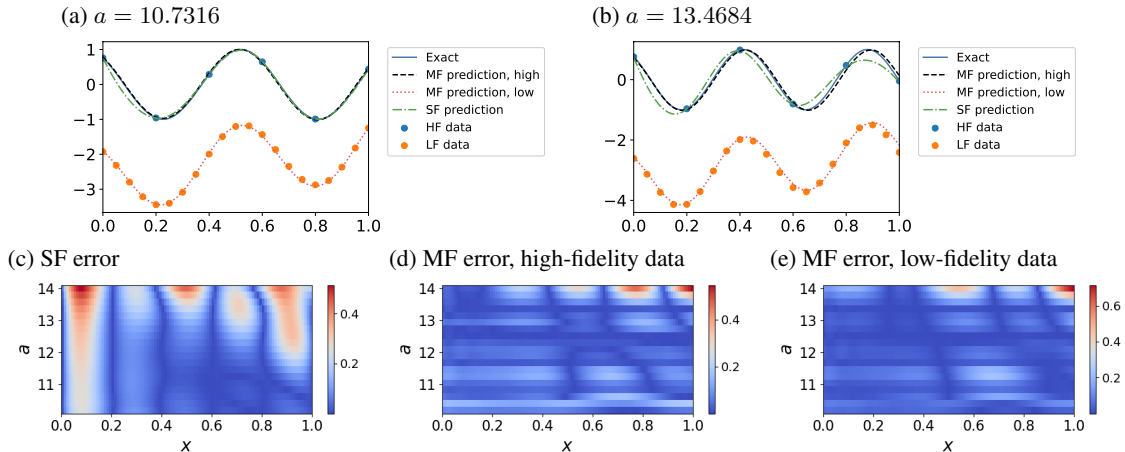


Figure 3: Data-driven multifidelity: one-dimensional, correlation with u . (a-b) Results of the single fidelity and multifidelity predictions of the high-fidelity data. (c) Single-fidelity relative error as a function of a and x , (d) multifidelity high-fidelity prediction relative error as a function of a and x , and (e) multifidelity low-fidelity prediction relative error as a function of a and x .

2.3 Two-dimensional, linear correlation

We consider a two-dimensional problem with a linear correlation between the low-fidelity and high-fidelity data:

$$z_L(u)(x, y) = \cos(u) \cos(y) + x \quad (24)$$

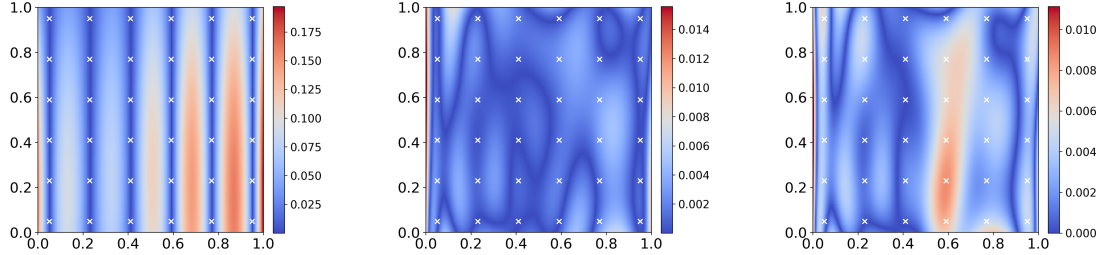
$$z_H(u)(x, y) = \cos(u) \cos(y) \quad (25)$$

$$u = ax - 4 \quad (26)$$

for $x, y \in [0, 1]$ and $a \in [8, 10]$. We have $z_H(u)(x, y) = z_L(u)(x, y) - x$ (see Fig. 16 in Appendix). The training parameters are given in Tab.5 (see Appendix B.3), and the results are given in Fig. 4. Note that the multifidelity prediction results in absolute errors approximately one order of magnitude smaller than the single fidelity prediction. The linear correlation found is:

$$\mathcal{F}_l(u)(x, y) = 0.9973\mathcal{F}_{LF}(u)(x, y) - 0.9392x - 0.0039y - 0.0032x\mathcal{F}_{LF}(u)(x, y) - 0.0048y\mathcal{F}_{LF}(u)(x, y) - 0.0256. \quad (27)$$

(a) $a = 8.5211$



(b) $a = 9.5737$

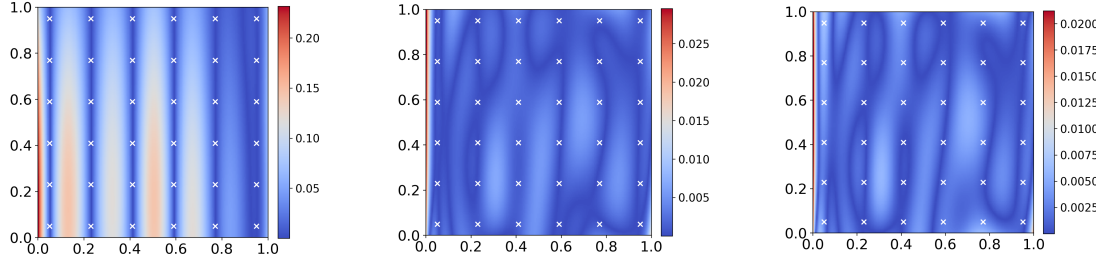


Figure 4: Data-driven multifidelity: two-dimensional, linear correlation. (a) Absolute error of the high-fidelity prediction, multifidelity prediction of the high-fidelity data, and multifidelity prediction of the low-fidelity data for $a = 8.5211$. (b) Absolute error of the high-fidelity prediction, multifidelity prediction of the high-fidelity data, and multifidelity prediction of the low-fidelity data for $a = 9.5737$. The high-fidelity data points are shown in white for illustration.

2.4 Two-dimensional, nonlinear correlation

We consider a two-dimensional problem with a nonlinear correlation between the low-fidelity and high-fidelity data:

$$z_L(u)(x, y) = \cos(u) \cos(y) + x \quad (28)$$

$$z_H(u)(x, y) = \cos(u) \cos(y)^2 \quad (29)$$

$$u = ax - 4 \quad (30)$$

for $x, y \in [0, 1]$ and $a \in [8, 10]$. The training parameters are given in Tab. 6, and the low- and high-fidelity functions are plotted in Fig. 18 (see Appendix B.4). The results are given in Fig. 5. Even though the correlation is complex and nonlinear, the composite multifidelity DeepONet improves the predictions by up to an order of magnitude. While the single fidelity method agrees well at locations where training data is provided, overfitting results in large errors in areas where there is no training data. In Fig. 6 we show the outputs of the linear and nonlinear DeepONets for two input functions. The correction learned by the nonlinear DeepONet is smaller in magnitude than the output of the linear DeepONet, representing a small nonlinear correction to the linear correlation.

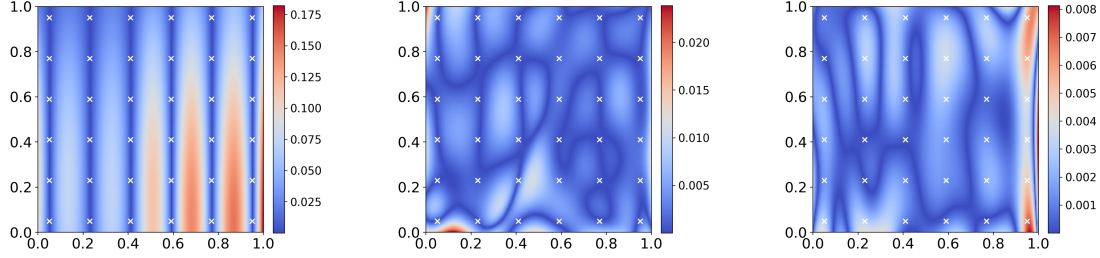
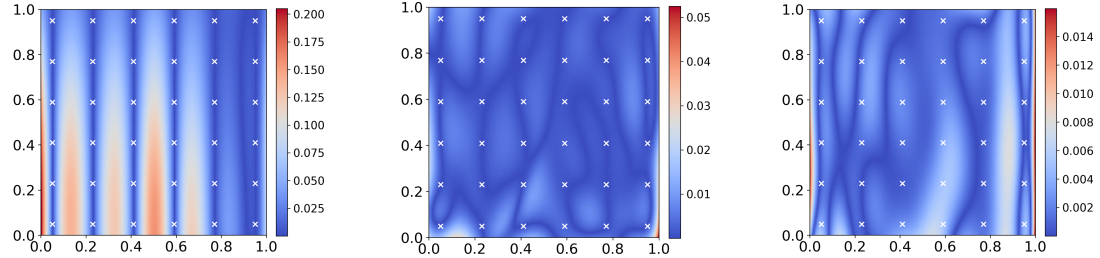
(a) $a = 8.5211$

 (b) $a = 9.5737$


Figure 5: Data-driven multifidelity: two-dimensional, nonlinear correlation. (a) Absolute error of the high-fidelity prediction, multifidelity prediction of the high-fidelity data, and multifidelity prediction of the low-fidelity data for $a = 8.5211$. (b) Absolute error of the high-fidelity prediction, multifidelity prediction of the high-fidelity data, and multifidelity prediction of the low-fidelity data for $a = 9.5737$. The high-fidelity data points are shown in white for clarity.

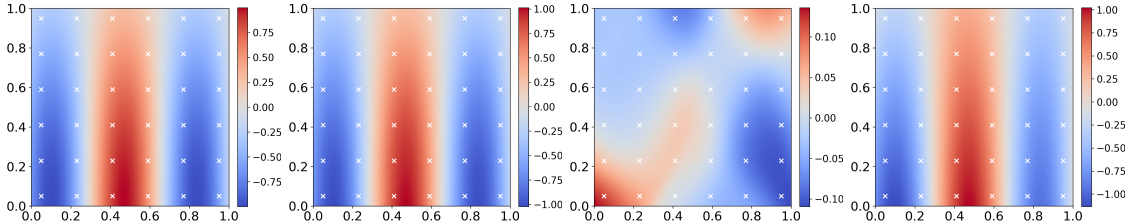
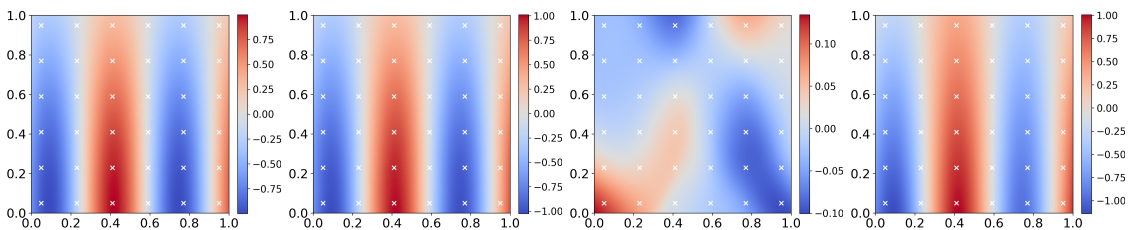
 (a) $a = 8.5211$

 (b) $a = 9.5737$


Figure 6: Data-driven multifidelity: two-dimensional nonlinear correlation. From left to right: exact high-fidelity solution, multifidelity DeepONet prediction, multifidelity DeepONet nonlinear correlation, and multifidelity DeepONet linear correlation. The high-fidelity data points are shown in white for clarity.

2.5 Ice-sheet modeling

To provide an example of the data-driven multifidelity method applied to complex problems, here we consider ice-sheet modeling. Ice-sheet models are an important component of earth system models and are critical for computing projections of sea-level rise. In order to quantify the uncertainty of sea-level projections, the ice-sheet models need to be evaluated a large number of times. At present, the high computational cost of these models hinders the ability to perform

uncertainty quantification and DeepONets can be used to overcome this issue by generating inexpensive surrogates of ice-sheet models. The proposed multifidelity DeepONet framework can be used to leverage the available hierarchy of ice-sheet models [e.g. 15, 32, 40] of different fidelity and cost, and significantly reduce the cost of generating model data. This hierarchy of models is based on different approximations of the Stokes equation that exploit the shallow nature of ice sheets (see Appendix D). In this work we will focus on two ice-sheet models, the low-fidelity (zeroth-order¹) *Shallow Shelf Approximation* (SSA) [30], and the higher-fidelity model, *MONo-Layer Higher-Order model* (MOLHO) [13]. In addition to considering different models, we will also consider the same model at different resolutions.

2.5.1 Data generation

The basal friction field β is one of the biggest controls on ice velocity. It cannot be measured directly and it is typically estimated by solving a PDE-constrained optimization problem [e.g. 33] to assimilate observation of the surface ice velocity. As a result, the basal friction field is affected by both uncertainties in the observations and in the uncertainties in the model. While it is possible to characterize the probability distribution for β using a Bayesian inference approach [e.g. 34], here we adopt a simplified log-normal distribution for β . We write the basal friction field as $\beta = \exp(\gamma)$, where γ is normally distributed as

$$\gamma \sim \mathcal{G}(\log(\beta_{\text{opt}}), k_l), \text{ and } k_l(\mathbf{x}_1, \mathbf{x}_2) = a \exp\left(-\frac{|\mathbf{x}_1 - \mathbf{x}_2|^2}{2l^2}\right). \quad (31)$$

Here β_{opt} is the nominal value of β , often obtained by assimilating the observed velocities [33], l the correlation length and a a scaling factor.

As a step towards enabling efficient uncertainty quantification, we use a DeepONet to find the depth-averaged velocity \bar{u} for an ice sheet as a function of the basal friction and ice-sheet thickness. In order to create data for training the DeepONet we sample values for beta according to (31). For each sample β_i one can solve, with a numerical method, the coupled thickness-velocity problem, and obtain values for the ice thickness $H_i^k(x, y)$ and velocities $\bar{u}_i^k(x, y)$ at time t^k that can be used to train the DeepONet (see Fig. 7).

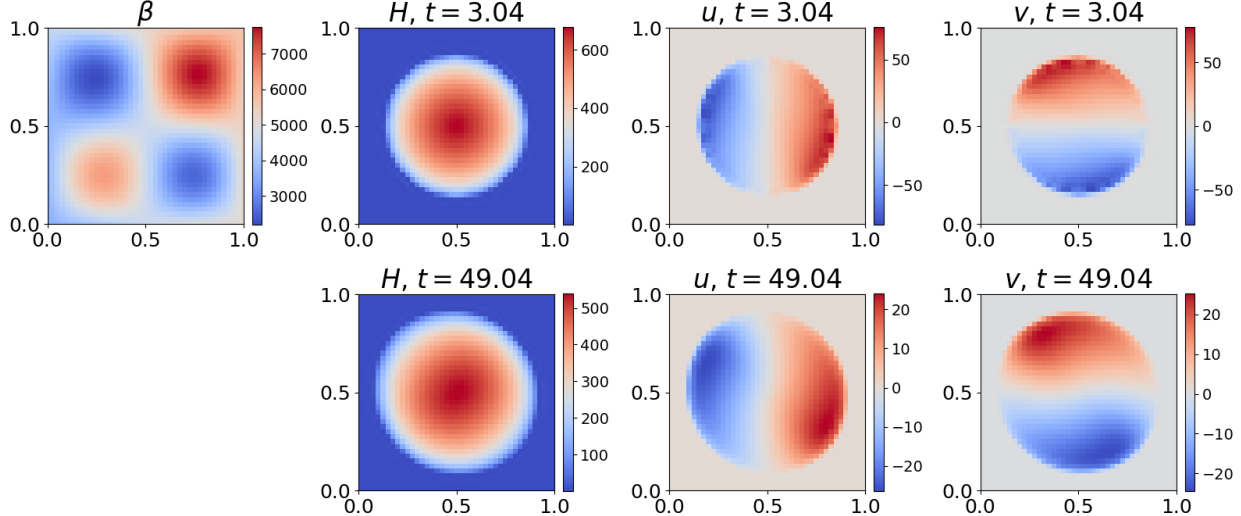


Figure 7: Data-driven multifidelity: multiresolution ice-sheet dynamics. Example of the ice-sheet dynamics from an SSA simulation with resolution 41x41 at times $t = 3.04$ yr and $t = 49.04$ yr. The basal friction is denoted by β (units: [Pa yr / m]), the ice thickness by H (units: [m]), and the x - and y - depth-averaged velocities by u and v (units: [m / yr]). The basal friction β is constant in time.

2.5.2 Multiresolution

We first consider the multiresolution case for the so-called Halfar dome [18] and we let the dome of ice deform under no external forcing. We generate two training sets using meshes of different resolution and running the problem forward in

¹Here the order of an approximation refers to the order of the terms, with respect to the aspect-ratio (thickness over horizontal length) of an ice sheet, that are retained in the approximation

time for 50 yrs for each β sampled from (31) with $l = 54$ km, $a = 1.0$, and $\beta_{\text{opt}} = 3000 \left(1 + \frac{1}{2} \sin\left(\frac{\pi x}{30\text{km}}\right) \sin\left(\frac{\pi y}{30\text{km}}\right)\right)$. The low-fidelity training set uses the SSA model on a coarse $P_L = 15 \times 15$ mesh. The high-fidelity training set uses the same SSA model but on a much finer $P_H = 41 \times 41$ mesh. Due to the size of the mesh, it is time demanding both to generate and to train on the full high-resolution training set.

We consider multiple cases of the single fidelity training with $N_H = 10$ and $N_H = 50$ high-fidelity 41x41 datasets, and the multifidelity case trained on $N_L = 100$ 15x15 low-fidelity datasets and $N_H = 10$ 41x41 high-fidelity datasets. We consider both hyperbolic tangent and ReLU activation functions. Due to the sharp gradients found in the height and velocity of the ice sheets at the border of the sheet, we find that the ReLU activation function performs better in some cases. For simplicity, the same activation function is used in both the low fidelity and nonlinear subnets in the multifidelity training. In this case, the nonlinear correlation does not necessarily demonstrate the sharp gradients present in the low- and high-fidelity data, so the performance with the ReLU activation function is similar to the performance with the hyperbolic tangent activation function. The training parameters are given in Tab. 7 and the computational cost is given in Tab. 8 in Appendix B.5. The testing errors are calculated by taking the mean mean squared error (MSE), defined as

$$E_1 = \frac{1}{N_H^T} \sum_{i=1}^{N_H^T} \frac{1}{P_H} \sum_{j=1}^{P_H} [\bar{u}(\beta_i, H_i)(\mathbf{x}_j) - \mathcal{F}_l(\beta_i, H_i)(\mathbf{x}_j) - \mathcal{F}_{nl}(\beta_i, H_i)(\mathbf{x}_j)]^2 \quad (32)$$

and mean relative L_2 error,

$$E_2 = \frac{1}{N_H^T} \sum_{i=1}^{N_H^T} \sqrt{\frac{\sum_{j=1}^{P_H} [\bar{u}(\beta_i, H_i)(\mathbf{x}_j) - \mathcal{F}_l(\beta_i, H_i)(\mathbf{x}_j) - \mathcal{F}_{nl}(\beta_i, H_i)(\mathbf{x}_j)]^2}{\sum_{j=1}^{P_H} [\bar{u}(\beta_i, H_i)(\mathbf{x}_j)]^2}}, \quad (33)$$

for $N_H^T = 50$ high-resolution 41x41 datasets not used in training, and are shown in Tab. 1. The errors from the single fidelity case with $N_H = 50$ datasets match the multifidelity case, although we note that this case requires five times more expensive high-resolution simulations to generate the training data. In comparison, the multifidelity approach achieves accurate results with only $N_H = 10$ high-resolution simulations (see Fig. 8).

Method	Mean MSE (Eq. 32)	Mean relative L_2 error (Eq. 33)
Single fidelity, $N_H = 10$, tanh	0.00237	0.24782
Single fidelity, $N_H = 50$, tanh	0.00225	0.22526
Single fidelity, $N_H = 10$, ReLU	0.15814	0.66923
Single fidelity, $N_H = 50$, ReLU	0.00012	0.05074
Multifidelity, $N_H = 10$, $N_L = 100$, tanh	5.1556×10^{-5}	0.03170
Multifidelity, $N_H = 10$, $N_L = 100$, ReLU	8.8973×10^{-5}	0.04442

Table 1: Data-driven multifidelity: multiresolution ice-sheet dynamics. Mean relative L_2 errors and mean MSEs for each case, tested over $N_H^T = 50$ testing sets.

2.5.3 Multiorder

We can also consider the case where we have two different models, a low-order and a high-order model, applied to the Humboldt glacier, Greenland. In this case, the low-order model is faster to run, so it is easier to generate a large amount of low-order data to represent the low-fidelity dataset. The high-order method is more time-consuming, so we use a small amount of high-order data in the high-fidelity dataset. For each sample of β , obtained sampling 31 with correlation length $l = 80$ km and scaling $a = 0.2$, the ice flow model is run forward in time for 100 yr, using a climate forcing generated accordingly to the *Representative Concentration Pathway 2.6* (see [20] for the problem definition and the data used including the nominal basal friction β_{opt}). We use $N_H = 20$ runs (corresponding to 20 samples of β) using MOLHO model as our high-fidelity dataset. The low-fidelity dataset has $N_L = 80$ runs of the SSA model. Both the high- and low-fidelity datasets use the same nonuniform mesh. Example output from the MOLHO simulations is shown in Fig. 9. The training parameters are given in Tab. 9 and the computational cost is given in Tab. 10 in Appendix B.6. The output from the single fidelity and multifidelity training is shown in Fig. 10. The single fidelity method has a mean relative L_2 error of 1.1005, while the multifidelity method has a mean relative L_2 error of 0.3676 across five simulations in the high-fidelity test set.

3 Physics-informed multifidelity DeepONets

In this section, we consider the application of the multifidelity method to cases where we have low-fidelity data and knowledge of the physics of the system. In particular, the high-fidelity network is trained without paired input-output

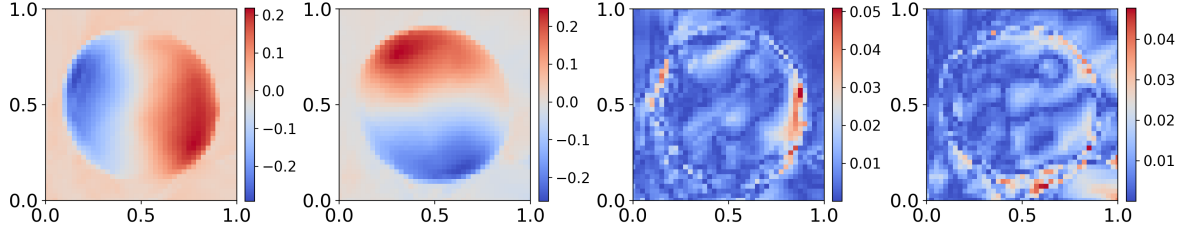
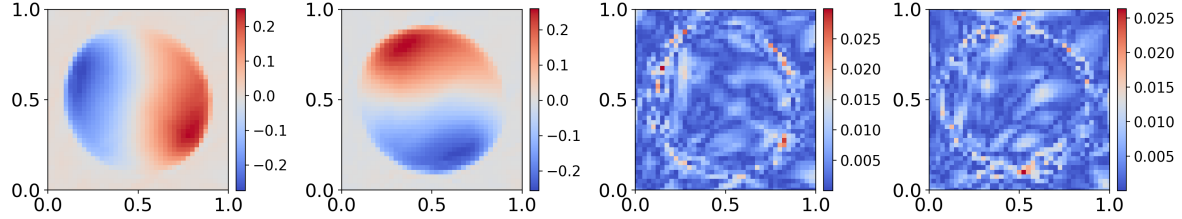
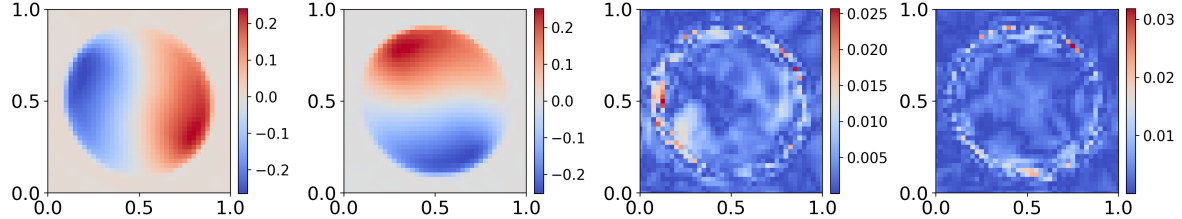
(a) Single fidelity, $N_H = 10$ (b) Single fidelity, $N_H = 50$ (c) Multifidelity, $N_H = 10, N_L = 100$ 

Figure 8: Data-driven multifidelity: multiresolution ice-sheet dynamics. Predictions at time $t = 49.04$ yr for the depth-averaged velocity components u and v , and pointwise error for u and v are shown from left to right, units: [m / yr]. (a) DeepONet single fidelity prediction with 10 samples in the training set. (b) DeepONet single fidelity prediction with 50 samples in the training set. (b) DeepONet multifidelity prediction with 100 samples in the low-fidelity training set and 10 samples in the high-fidelity training set. All cases here use the `relu` activation function.

observations. In practice, it is often inexpensive to generate low-fidelity solutions to a PDE with a numerical method, but the numerical method may be too expensive to run at high resolution, or may be low order and miss important features of the full solution. Here, we show we can use the low-fidelity numerical data as the input to the low-fidelity network, and then correct the output using physics-informed DeepONets to result in more accurate outputs. We consider first a one-dimensional case with a nonlinear correlation between the low-fidelity data and the ODE solution. We then consider the viscous Burgers equation, where the low-fidelity data is provided by a numerical solver both with and without noise added.

3.1 One-dimensional, nonlinear correlation

We consider the case given by:

$$y_L(a)(x) = \cos(4\pi x + a)^2 \quad (34)$$

$$\frac{\partial}{\partial x} y_H(a)(x) = -4\pi \sin(4\pi x + a) \quad (35)$$

$$y_H(a)(0) = \cos(a) \quad (36)$$

$$(37)$$

for $x \in [0, 1]$ and $a \in [0, 5]$. We note that the exact solution to the ODE is $y_H(a)(x) = \cos(4\pi x + a)$. Parameters are given in Tab. 11 (see Appendix B.7) and results in Fig. 11. The testing set consists of 20 input values of $a \in [.0125, 4.975]$ and 101 values of $x \in [0, 1]$. On the test set, the mean MSE of the single fidelity prediction is 0.61648 and the mean MSE of the high-fidelity MF prediction is 0.16232.

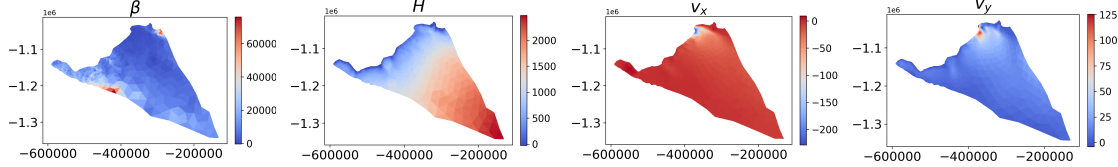
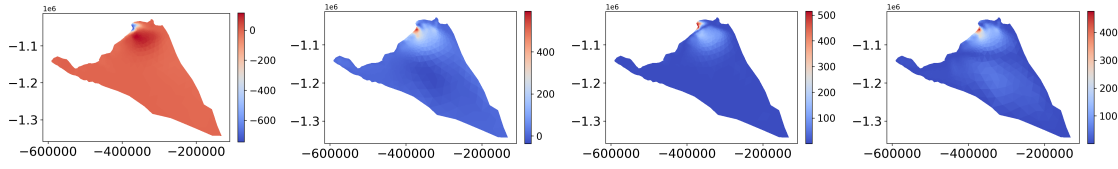


Figure 9: Data-driven multifidelity: multiorder ice sheet dynamics. Example of the ice-sheet dynamics from an MOLHO simulation with 1426 points at times $t = 99.0$ yr. From left to right: the basal friction β [Pa yr / m], the ice thickness H [m], and the depth-averaged velocity components v_x and v_y [m / yr].

(a) Single fidelity



(b) Multifidelity

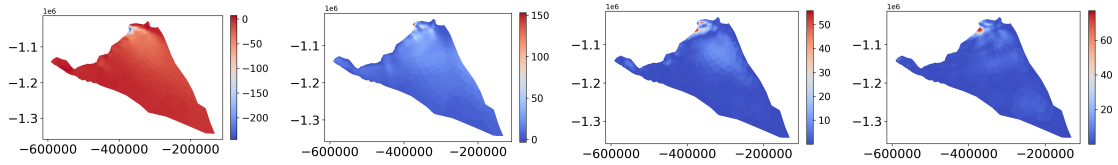


Figure 10: Data-driven multifidelity: multiorder ice-sheet dynamics. Output from the test set for the single fidelity (a) and multifidelity (b) training at time $t = 99.0$ yr. From left to right we show, v_x , v_y the pointwise error in v_x , and the pointwise error in v_y , (units: [m / yr]).

3.2 Viscous Burgers Equation

We consider the viscous one-dimensional Burgers equation with periodic boundary conditions:

$$\frac{ds}{dt} + s \frac{ds}{dx} - \nu \frac{d^2s}{dx^2} = 0, \quad (x, t) \in (0, 1) \times (0, 1] \quad (38)$$

$$s(x, 0) = u(x), \quad x \in (0, 1), \quad (39)$$

$$s(0, t) = s(1, t), \quad t \in (0, 1), \quad (40)$$

$$\frac{ds}{dx}(0, t) = \frac{ds}{dx}(1, t), \quad t \in (0, 1) \quad (41)$$

where ν is the viscosity. The initial condition, $u(x)$, is generated from a Gaussian random field (GRF). To generate the training data we follow the procedure in [47, 46, 35] and generate $N = 1500$ samples from a Gaussian random field $\sim \mathcal{N}(0, 25^2(-\Delta + 5^2I)^{-4})$. For the physics-informed cases, the initial condition is sampled at $P_{IC} = 100$ uniformly spaced locations on $x = [0, 1]$. The boundary conditions are randomly sampled at $P_{BC} = 100$ locations on $(x, t) = (0, t)$ and $(x, t) = (1, t)$. The residual is evaluated on $P_p = 2,500$ randomly sampled collocation points from the interior of the domain. The training is completed with $N_H = 1000$ samples, and the results are tested on the remaining 500 samples. We consider three cases: data-only, using the low-fidelity training set, physics-only, using the physics-informed training set, and multifidelity, which combines the low-fidelity training set and physics-informed training set.

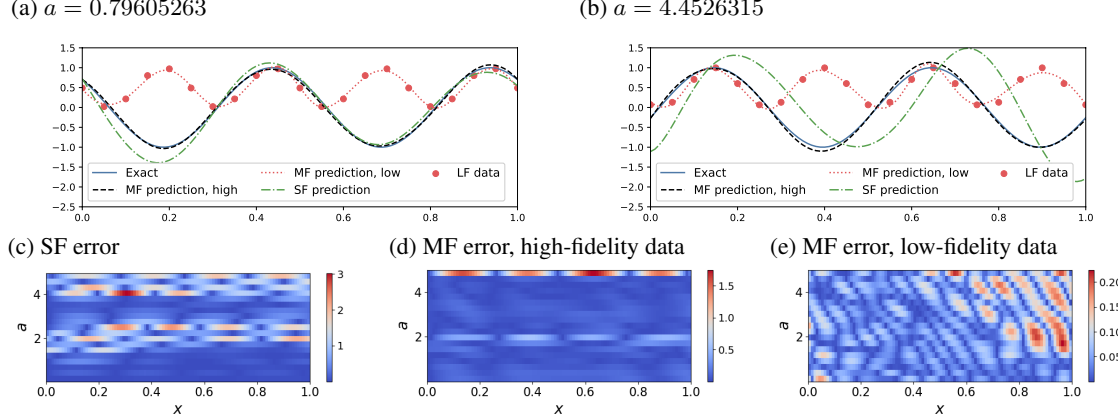


Figure 11: Physics-informed multifidelity: nonlinear correlation. (a) Results of the single fidelity and multifidelity predictions of the high- and low-fidelity data with $a = 0.79605263$. (b) Results of the single fidelity and multifidelity predictions of the high- and low-fidelity data with $a = 4.4526315$. (c) Single-fidelity error as a function of a and x , (d) multifidelity high-fidelity prediction error as a function of a and x , and (e) multifidelity low-fidelity prediction error as a function of a and x .

The low-fidelity data for the multifidelity and data-only training are generated by solving Burgers equation with the Chebfun package [14] with a spectral Fourier discretization and a fourth-order stiff time-stepping scheme (ETDRK4) [8] with a timestep $\Delta t = 5 \times 10^{-3}$ for $\nu = 10^{-2}$ and $\nu = 10^{-3}$ and $\Delta t = 10^{-4}$ for $\nu = 10^{-4}$. The initial condition is sampled on $M_L = 21$ uniformly spaced locations on $x = [0, 1]$, and snapshots of the solution are saved every $\delta t = 0.05$, to give data on a 21×21 grid. The high-fidelity test data is generated with the same scheme with time step $\Delta t = 10^{-4}$, but the initial condition is sampled at $P = 101$ locations and the time snapshots are taken every $\delta t = 0.01$, to give data on a 101×101 grid. We take the number of low-fidelity training sets to be either $N_L = 200$ or $N_L = 1000$. We also consider a second low-fidelity dataset, generated by adding Gaussian white noise generated by a normal distribution with variance $\sigma^2 = 4 \times 10^{-4}$ and mean 0 to each point in the 21×21 output. This is referred to as training “with noise”.

The multifidelity loss function is given by Eq. 15. For the data-only case, $\lambda_1 = \lambda_3 = \lambda_4 = \lambda_5 = \lambda_6 = 0$. In the physics-only case, $\lambda_2 = \lambda_3 = \lambda_4 = 0$. Across all cases, the non-zero weights are kept fixed: $\lambda_1 = 10$, $\lambda_2 = 1$, $\lambda_3 = 10^{-6}$, $\lambda_4 = 10^{-6}$, $\lambda_5 = 20$, and $\lambda_6 = 1$. The other hyperparameters are given in Tab. 12 (see Appendix B.8). In the multifidelity training, the low-fidelity output is sampled on an 11×11 mesh to use as input to the physics-informed nonlinear branch net.

The results of the physics-only, data-only, and multifidelity training are given in Tab. 2. We can see that the data-only predictions are very accurate, especially when no noise is included. With noise, the data-only predictions show larger relative errors for small values of the viscosity. As reported in [47, 46], at the smallest value of the viscosity the physics-only training has a large relative error. In comparison, the multifidelity method is able to significantly reduce the relative error for $\nu = 10^{-4}$. Interestingly, the results of the multifidelity method with and without noise are quite similar, indicating that the multifidelity method can overcome noisy low-fidelity data by correcting the low-fidelity output by enforcing the PDE. When the size of the low-fidelity training set is reduced for $\nu = 10^{-4}$ the data-only errors increase significantly due to the decrease in available training data. This is especially noticeable for the data-only training with noisy data. In contrast, the relative error with the multifidelity method has a smaller increase with the decrease in the size of the low-fidelity training set. Results of typical outputs from the training for $\nu = 10^{-3}$ and $\nu = 10^{-4}$ with $N_L = 1000$ are given in Fig. 12. At the lowest viscosity, the physics-only method under predicts the steep gradient while the data-only method overshoots the gradient. The errors are concentrated in the area with the highest gradients. In Fig. 13 we show the results of training with the noisy low-fidelity dataset with $N_L = 200$ and $N_L = 1000$ for $\nu = 10^{-4}$. With the larger number of low-fidelity training sets, the multifidelity output is comparable to the multifidelity DeepONet trained with data without noise. The data-only error increases significantly with fewer low-fidelity noisy training sets. A table of the computational cost for the different methods is given in Tab. 13 (Appendix B.8). While the multifidelity training comes at increased computational cost over the physics-only model, due to the additional computations needed for the three subnetworks, the additional training cost results in higher accuracy.

Parameters	$\nu = 10^{-2}$ $N_L = 1000$	$\nu = 10^{-3}$ $N_L = 1000$	$\nu = 10^{-4}$ $N_L = 1000$	$\nu = 10^{-4}$ $N_L = 200$
Data-only	$1.02\% \pm 0.81\%$	$2.46\% \pm 1.67\%$	$7.64\% \pm 2.66\%$	$13.57\% \pm 7.40\%$
Data-only with noise	$4.44\% \pm 3.48\%$	$6.50\% \pm 3.45\%$	$10.63\% \pm 5.54\%$	$26.11\% \pm 15.38\%$
Physics-only	$3.97\% \pm 5.71\%$	$8.66\% \pm 6.47\%$	$23.63\% \pm 10.22\%$	—
Multifidelity	$2.81\% \pm 1.81\%$	$6.25\% \pm 2.20\%$	$7.05\% \pm 3.01\%$	$9.70\% \pm 4.60\%$
Multifidelity with noise	$2.89\% \pm 1.70\%$	$6.65\% \pm 2.48\%$	$7.03\% \pm 3.10\%$	$10.16\% \pm 5.55\%$

Table 2: Physics-informed multifidelity: viscous Burgers equation mean relative L_2 errors. The physics-only and multifidelity cases all use $N_H = 1000$. Note that the physics-only case does not use any low-fidelity data.

4 Discussion

In this work, we presented a new composite DeepONet framework for learning operators with multifidelity data. The method uses a large set of inexpensive low-fidelity data and either a small amount of high-fidelity data or enforces physics on the system. In multiphysics and complex system problems it is common to have low order numerical solvers available, but attaining high order measurements or simulations is costly. This method allows for using both low- and high-fidelity data to achieve higher accuracy. When PDEs describing the system are known, the physics-informed multifidelity DeepONet allows for training with low-fidelity data and using a physics-informed DeepONet for the high-fidelity training.

Many extensions of this work are possible to accommodate the data available for novel applications. For example, if a solver for the low-fidelity data is available, either through a surrogate model such as a DeepONet or through a numerical method, this solver can be incorporated instead of the low-fidelity subnetwork presented here. A discussion of this case is given in Appendix C. The multifidelity DeepONet framework can also be used to include more than two fidelities of data by incorporating additional fidelity data into the branch net for training. If partial knowledge of the physics is available, the loss function could be modified to enforce the incomplete physical model on the low-fidelity output, then correct the incomplete model with data-driven high-fidelity DeepONets. This case is particularly applicable in cases such as fluid modeling, where sparse but high-fidelity experimental data is available. Future extensions of this work include incorporating weighting schemes in the loss function to improve training, along the lines of [46].

5 Acknowledgements

The authors wish to thank P. Perdikaris, Q. He, and L. Lu for helpful discussions, K. C. Sockwell for co-developing the ice-sheet code, and T. Hillebrand for generating the Humboldt grid.

The work is supported by the U.S. Department of Energy, Advanced Scientific Computing Research program, under the Physics-Informed Learning Machines for Multiscale and Multiphysics Problems (PhILMs) project and under the SciDAC-BER Probabilistic Sea Level Projections from Ice-Sheets and Earth System Models (ProSPect) partnership.

Pacific Northwest National Laboratory (PNNL) is a multi-program national laboratory operated for the U.S. Department of Energy (DOE) by Battelle Memorial Institute under Contract No. DE-AC05-76RL01830. The computational work was performed using PNNL Institutional Computing at Pacific Northwest National Laboratory.

Sandia National Laboratories is a multimission laboratory managed and operated by National Technology and Engineering Solutions of Sandia, LLC., a wholly owned subsidiary of Honeywell International, Inc., for the U.S. Department of Energy's National Nuclear Security Administration under contract DE-NA-0003525.

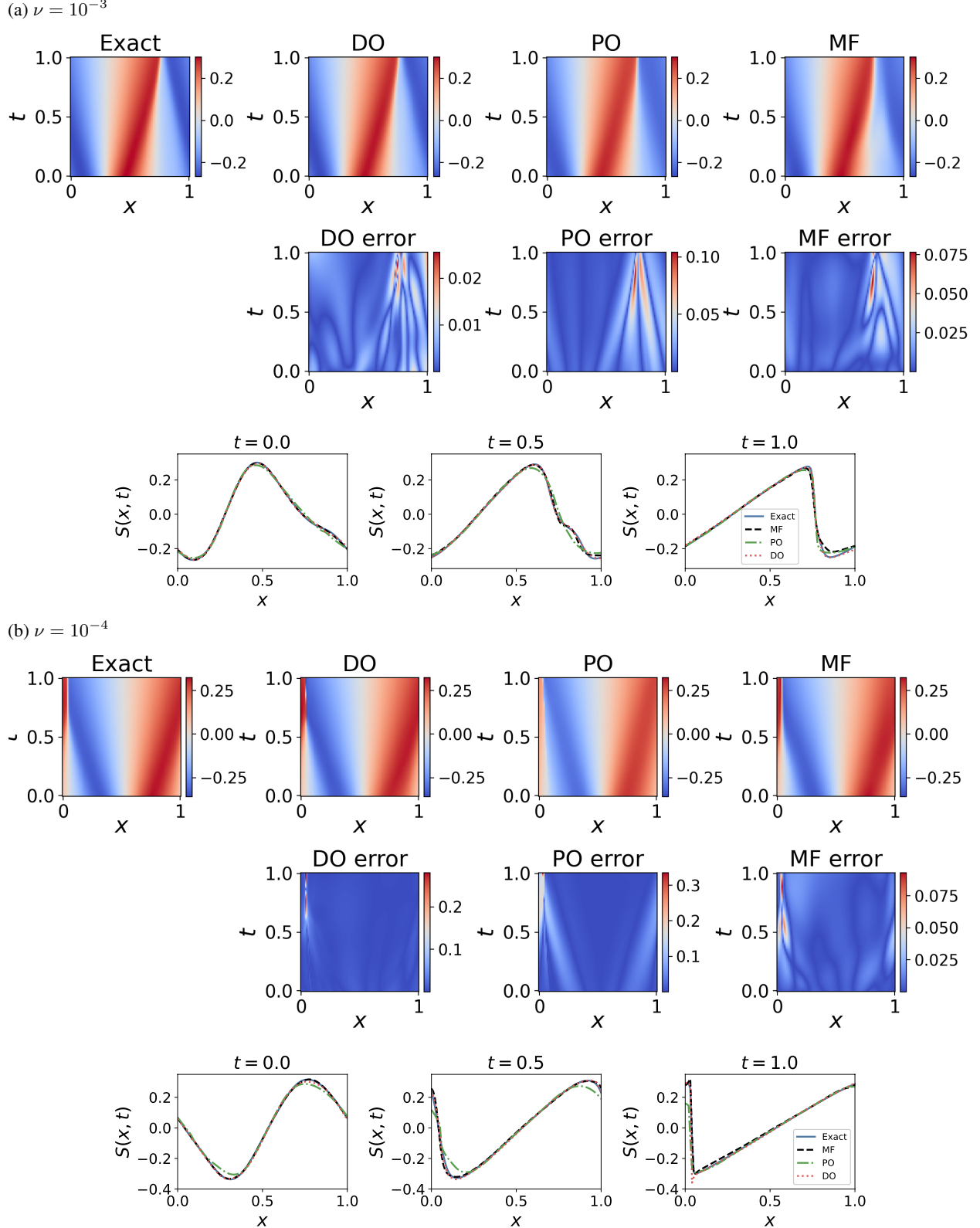


Figure 12: Physics-informed multifidelity: viscous Burgers equation. Exact solution and results from the data-only training (DO), physics-only training (PO), and multifidelity training (MF) for (a) $\nu = 10^{-3}$ and (b) $\nu = 10^{-4}$. The errors are the absolute errors between the exact solution and the method output. These examples use the low-fidelity dataset without noise.

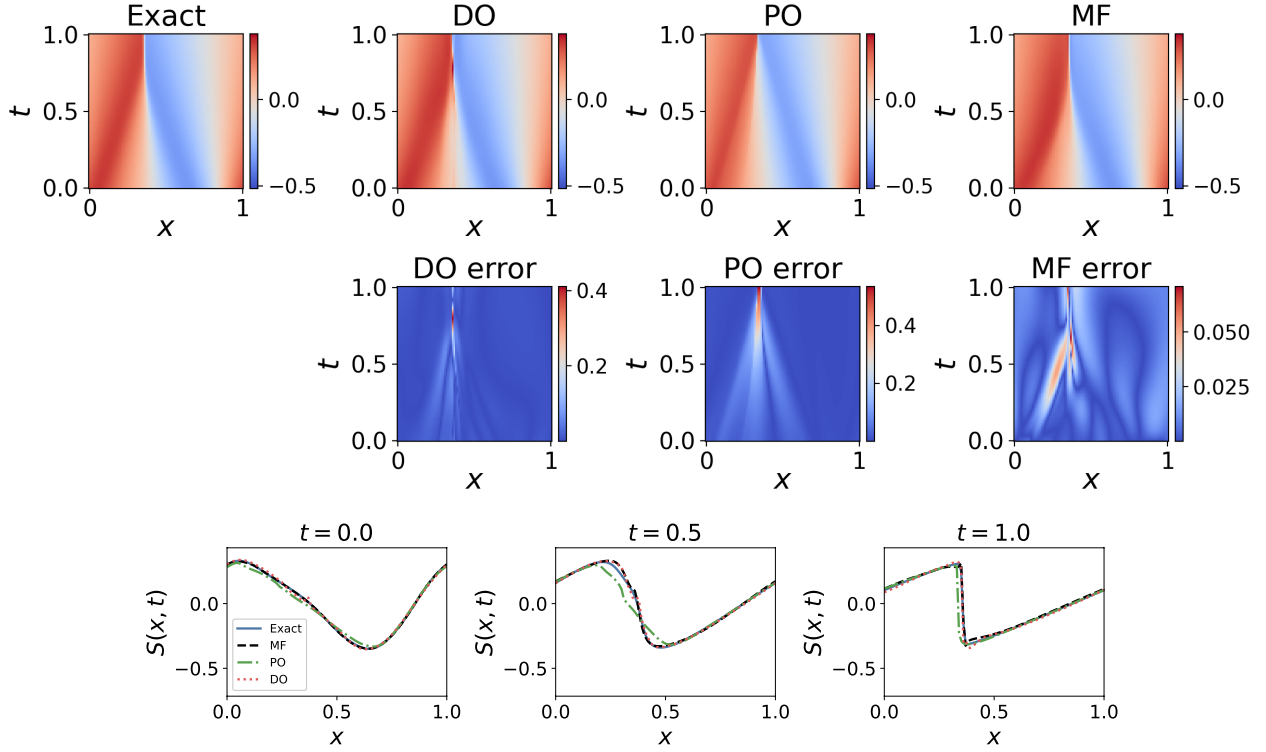
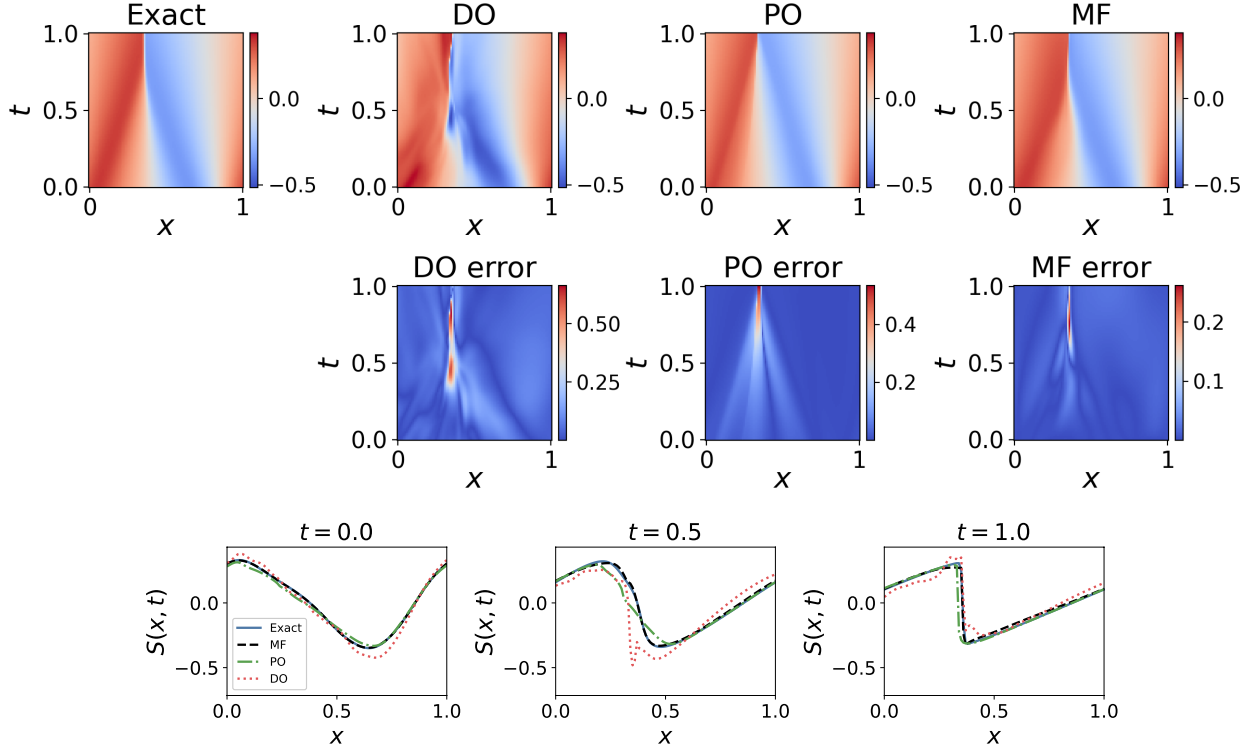
(a) $\nu = 10^{-4}$, $N_L = 1000$ (b) $\nu = 10^{-4}$, $N_L = 200$ 

Figure 13: Physics-informed multifidelity: viscous Burgers equation. Exact solution and results from the data-only training (DO), physics-only training (PO), and multifidelity training (MF) for (a) $\nu = 10^{-4}$ with $N_L = 1000$ and (b) $\nu = 10^{-4}$ with $N_L = 200$. The errors are the absolute errors between the exact solution and the method output. These examples use the low-fidelity dataset with noise.

References

- [1] H. Babaee et al. “A multifidelity framework and uncertainty quantification for sea surface temperature in the Massachusetts and Cape Cod Bays”. In: *Earth and Space Science* 7.2 (2020), e2019EA000954.
- [2] A. D. Back and T. Chen. “Universal approximation of multiple nonlinear operators by neural networks”. In: *Neural Computation* 14.11 (2002), pp. 2561–2566.
- [3] A. G. Baydin et al. “Automatic differentiation in machine learning: a survey”. In: *Journal of Machine Learning Research* 18 (2018), pp. 1–43.
- [4] J. Bradbury et al. *JAX: composable transformations of Python+NumPy programs*. Version 0.2.5. 2018. URL: <http://github.com/google/jax>.
- [5] S. Chakraborty. “Transfer learning based multi-fidelity physics informed deep neural network”. In: *Journal of Computational Physics* 426 (2021), p. 109942.
- [6] T. Chen and H. Chen. “Approximation capability to functions of several variables, nonlinear functionals, and operators by radial basis function neural networks”. In: *IEEE Transactions on Neural Networks* 6.4 (1995), pp. 904–910.
- [7] T. Chen and H. Chen. “Universal approximation to nonlinear operators by neural networks with arbitrary activation functions and its application to dynamical systems”. In: *IEEE Transactions on Neural Networks* 6.4 (1995), pp. 911–917.
- [8] S. M. Cox and P. C. Matthews. “Exponential time differencing for stiff systems”. In: *Journal of Computational Physics* 176.2 (2002), pp. 430–455.
- [9] S. De and A. Doostan. “Neural network training using ℓ_1 -regularization and bi-fidelity data”. In: *Journal of Computational Physics* (2022), p. 111010.
- [10] S. De et al. “Bi-fidelity Modeling of Uncertain and Partially Unknown Systems using DeepONets”. In: *arXiv preprint arXiv:2204.00997* (2022).
- [11] S. De et al. “On transfer learning of neural networks using bi-fidelity data for uncertainty propagation”. In: *International Journal for Uncertainty Quantification* 10.6 (2020).
- [12] P. C. Di Leoni et al. “Deepenet prediction of linear instability waves in high-speed boundary layers”. In: *arXiv preprint arXiv:2105.08697* (2021).
- [13] T. Dias dos Santos, M. Morlighem, and D. Brinkerhoff. “A new vertically integrated MOOno-Layer Higher-Order (MOLHO) ice flow model”. In: *The Cryosphere* 16.1 (2022), pp. 179–195. DOI: 10.5194/tc-16-179-2022.
- [14] T. A. Driscoll, N. Hale, and L. N. Trefethen. *Chebfun guide*. 2014.
- [15] J. K. Dukowicz, S. F. Price, and W. H. Lipscomb. “Consistent approximations and boundary conditions for ice-sheet dynamics from a principle of least action”. In: *Journal of Glaciology* 56.197 (2010), pp. 480–496. ISSN: 0022-1430. DOI: 10.3189/002214310792447851.
- [16] S. Goswami et al. “A physics-informed variational DeepONet for predicting the crack path in brittle materials”. In: *arXiv preprint arXiv:2108.06905* (2021).
- [17] A. Griewank et al. “On automatic differentiation”. In: *Mathematical Programming: recent developments and applications* 6.6 (1989), pp. 83–107.
- [18] P. Helffer. “On the dynamics of the ice sheets 2”. In: *Journal of Geophysical Research: Oceans* 88.C10 (1983), pp. 6043–6051. DOI: <https://doi.org/10.1029/JC088iC10p06043>.
- [19] K. Harada, D. Rajaram, and D. N. Mavris. “Application of Multi-Fidelity Physics-Informed Neural Network on Transonic Airfoil using Wind Tunnel Measurements”. In: *AIAA SCITECH 2022 Forum*. 2022, p. 0386.
- [20] T. R. Hillebrand et al. “The contribution of Humboldt Glacier, North Greenland, to sea-level rise through 2100 constrained by recent observations of speedup and retreat”. In: *The Cryosphere Discussions* 2022 (2022), pp. 1–33. DOI: 10.5194/tc-2022-20.
- [21] A. D. Jagtap, D. Mitsotakis, and G. E. Karniadakis. “Deep learning of inverse water waves problems using multi-fidelity data: Application to Serre–Green–Naghdi equations”. In: *Ocean Engineering* 248 (2022), p. 110775.
- [22] S. Karumuri et al. “Simulator-free solution of high-dimensional stochastic elliptic partial differential equations using deep neural networks”. In: *Journal of Computational Physics* 404 (2020), p. 109120.
- [23] I. E. Lagaris, A. Likas, and D. I. Fotiadis. “Artificial neural networks for solving ordinary and partial differential equations”. In: *IEEE transactions on neural networks* 9.5 (1998), pp. 987–1000.
- [24] C. Lin et al. “A seamless multiscale operator neural network for inferring bubble dynamics”. In: *Journal of Fluid Mechanics* 929 (2021).
- [25] D. Liu and Y. Wang. “Multi-fidelity physics-constrained neural network and its application in materials modeling”. In: *Journal of Mechanical Design* 141.12 (2019).

[26] L. Lu, P. Jin, and G. E. Karniadakis. “Deeponet: Learning nonlinear operators for identifying differential equations based on the universal approximation theorem of operators”. In: *arXiv preprint arXiv:1910.03193* (2019).

[27] L. Lu et al. “Learning nonlinear operators via DeepONet based on the universal approximation theorem of operators”. In: *Nature Machine Intelligence* 3.3 (2021), pp. 218–229.

[28] X. Meng and G. E. Karniadakis. “A composite neural network that learns from multi-fidelity data: Application to function approximation and inverse PDE problems”. In: *Journal of Computational Physics* 401 (2020), p. 109020.

[29] X. Meng et al. “A fast multi-fidelity method with uncertainty quantification for complex data correlations: Application to vortex-induced vibrations of marine risers”. In: *Computer Methods in Applied Mechanics and Engineering* 386 (2021), p. 114212.

[30] L. W. Morland and I. R. Johnson. “Steady Motion of Ice Sheets”. In: *Journal of Glaciology* 25.92 (1980), pp. 229–246. DOI: 10.3189/S0022143000010467.

[31] M. Penwarden et al. “Multifidelity Modeling for Physics-Informed Neural Networks (PINNs)”. In: *Journal of Computational Physics* 451 (2022), p. 110844.

[32] M. Perego, M. Gunzburger, and J. Burkardt. “Parallel finite-element implementation for higher-order ice-sheet models”. In: *Journal of Glaciology* 58.207 (2012), pp. 76–88. DOI: 10.3189/2012JoG11J063.

[33] M. Perego, S. Price, and G. Stadler. “Optimal initial conditions for coupling ice sheet models to Earth system models”. In: *Journal of Geophysical Research Earth Surface* 119 (2014), pp. 1–24. DOI: 10.1002/2014JF003181. Received.

[34] N. Petra et al. “A Computational Framework for Infinite-Dimensional Bayesian Inverse Problems, Part II: Stochastic Newton MCMC with Application to Ice Sheet Flow Inverse Problems”. In: *SIAM Journal on Scientific Computing* 36.4 (2014), A1525–A1555. DOI: 10.1137/130934805.

[35] Predictive Intelligence Lab. *Physics informed DeepONets*. URL: <https://github.com/PredictiveIntelligenceLab/Physics-informed-DeepONets/tree/main/Burger/Data>.

[36] D. C. Psichogios and L. H. Ungar. “A hybrid neural network-first principles approach to process modeling”. In: *AIChE Journal* 38.10 (1992), pp. 1499–1511.

[37] M. Raissi, P. Perdikaris, and G. E. Karniadakis. “Physics-informed neural networks: A deep learning framework for solving forward and inverse problems involving nonlinear partial differential equations”. In: *Journal of Computational physics* 378 (2019), pp. 686–707.

[38] R. Ranade, K. Gitushi, and T. Echekki. “Generalized joint probability density function formulation for turbulent combustion using DeepONet”. In: *arXiv preprint arXiv:2104.01996* (2021).

[39] F. Regazzoni et al. “A physics-informed multi-fidelity approach for the estimation of differential equations parameters in low-data or large-noise regimes”. In: (2021).

[40] A. Robinson, D. Goldberg, and W. H. Lipscomb. “A comparison of the stability and performance of depth-integrated ice-dynamics solvers”. In: *The Cryosphere* 16.2 (2022), pp. 689–709. DOI: 10.5194/tc-16-689-2022.

[41] M. Sharma Priyadarshini, S. Venturi, and M. Panesi. “Application of DeepONet to model inelastic scattering probabilities in air mixtures”. In: *AIAA AVIATION 2021 FORUM*. 2021, p. 3144.

[42] J. Sirignano and K. Spiliopoulos. “DGM: A deep learning algorithm for solving partial differential equations”. In: *Journal of computational physics* 375 (2018), pp. 1339–1364.

[43] D. H. Song and D. M. Tartakovsky. “Transfer Learning on Multi-Fidelity Data”. In: *Journal of Machine Learning for Modeling and Computing* 2 (2021).

[44] L. Sun et al. “Surrogate modeling for fluid flows based on physics-constrained deep learning without simulation data”. In: *Computer Methods in Applied Mechanics and Engineering* 361 (2020), p. 112732.

[45] S. Wang and P. Perdikaris. “Long-time integration of parametric evolution equations with physics-informed deeponets”. In: *arXiv preprint arXiv:2106.05384* (2021).

[46] S. Wang, H. Wang, and P. Perdikaris. “Improved architectures and training algorithms for deep operator networks”. In: *arXiv preprint arXiv:2110.01654* (2021).

[47] S. Wang, H. Wang, and P. Perdikaris. “Learning the solution operator of parametric partial differential equations with physics-informed DeepONets”. In: *Science advances* 7.40 (2021), eabi8605.

[48] X. Zhang et al. “Multi-fidelity deep neural network surrogate model for aerodynamic shape optimization”. In: *Computer Methods in Applied Mechanics and Engineering* 373 (2021), p. 113485.

A Notation and abbreviations

N_L	Number of low-fidelity input samples in the training data set
M_L	Number of locations for evaluating input samples to the low-fidelity network
P_L	Length of the low-fidelity output
N_H	Number of high-fidelity input samples in the training data set
M_H	Number of locations for evaluating input samples to the high-fidelity network
P_H	Length of the high-fidelity output
P_{BC}	Number of boundary points
P_p	Number of collocation points for evaluating the PDE residual
θ	All trainable parameters of the multifidelity DeepONet system
\mathbf{u}	An input function
$\mathcal{G}(\mathbf{u})(\mathbf{x})$	An operator
$\mathcal{G}^\theta(\mathbf{u})(\mathbf{x})$	A DeepONet representation of an operator
$\mathcal{F}_{LF}^\theta(\mathbf{u})(\mathbf{x})$	The output of the low-fidelity DeepONet
$\mathcal{F}_{nl}^\theta(\mathbf{u})(\mathbf{x})$	The output of the nonlinear DeepONet
$\mathcal{F}_l^\theta(\mathbf{u})(\mathbf{x})$	The output of the linear DeepONet
SSA	Shallow Shelf Approximation
MOLHO	Mono-Layer Higher-Order model
MSE	Mean squared error
ODE	Ordinary differential equation
PDE	Partial differential equation
DO	Data-only
PO	Physics-only
LF	Low-fidelity
HF	High-fidelity
MF	Multifidelity
SF	Single fidelity

B Training parameters

In this section we provide the training parameters used in each test case for reproducibility.

The learning rate is set with the `optimizers.exponential_decay` function in JAX [4], which requires three parameters given as: (initial value, decay steps, decay rate). All test cases are trained with the `adam` optimizer. Unless noted, we use the hyperbolic tangent activation function.

B.1 One-dimensional, jump function

Parameter	Value
LF data	$M_L = P_L = 38$
HF data	$M_H = P_H = 5$
Number of LF datasets	$N_L = 20$ values of a
Number of HF datasets	$N_H = 10$ values of a
λ_1	0.1
λ_2	1
λ_3	1×10^{-1}
λ_4	1×10^{-3}
SF learning rate	(1e-3, 2000, 0.9)
MF learning rate	(5e-4, 2000, 0.99)
SF network size	3 layers, 30 neurons
MF low-fidelity network size	3 layers, 40 neurons
MF linear network size	1 layer, 5 neurons
MF nonlinear network size	2 layers, 30 neurons

Table 3: Training parameters for the one-dimensional jump function.

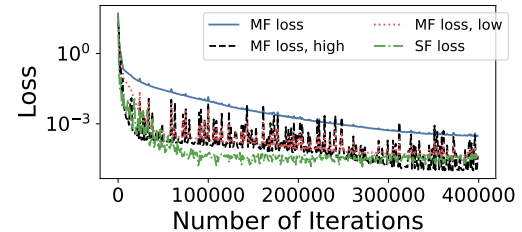


Figure 14: One-dimensional jump function training loss.

B.2 One-dimensional, correlation with u

Parameter	Value
LF data	$M_L = P_L = 21$
HF data	$M_H = P_H = 6$
Number of datasets	$N_L = N_H = 5$ values of a
λ_1	0.1
λ_2	1
λ_3	1×10^{-1}
λ_4	1×10^{-3}
SF learning rate	(1e-3, 2000, 0.9)
MF learning rate	(1e-3, 5000, 0.97)
SF network size	3 layers, 30 neurons
MF low-fidelity network size	3 layers, 30 neurons
MF linear network size	1 layer, 5 neurons
MF nonlinear network size	2 layers, 20 neurons

Table 4: Training parameters for the one-dimensional problem with correlation as a function of u .

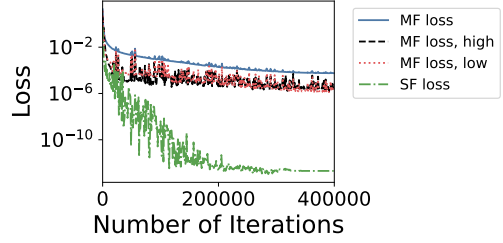


Figure 15: Training loss for the one-dimensional problem with correlation as a function of u .

B.3 Two-dimensional, linear correlation



Figure 16: (a) Exact low-fidelity function, z_L , and (b) exact high-fidelity function, z_H , for $a = 9.5737$.

Parameter	Value
LF data	$M_L = P_L = 21^2, x, y \in [.02, .98]$
HF data	$M_H = P_H = 6^2, x, y \in [.05, .95]$
Number of datasets	$N_L = N_H = 20$ values of a
λ_1	1
λ_2	1
λ_3	1×10^{-3}
λ_4	1×10^{-4}
SF learning rate	(1e-3, 5000, 0.9)
MF learning rate	(1e-3, 5000, 0.97)
SF network size	3 layers, 40 neurons
MF low-fidelity network size	3 layers, 30 neurons
MF linear network size	1 layer, 5 neurons
MF nonlinear network size	2 layers, 20 neurons

Table 5: Training parameters for the two-dimensional problem with linear correlation.

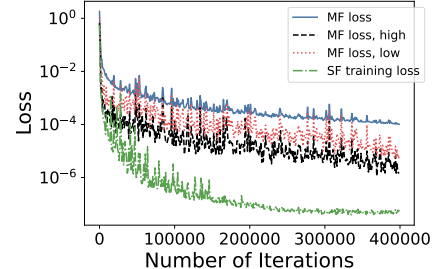


Figure 17: Training loss for the two-dimensional problem with linear correlation.

B.4 Two-dimensional, nonlinear correlation



Figure 18: (a) Exact low-fidelity function, z_L , and (b) exact high-fidelity function, z_H , for $a = 8.5211$.

Parameter	Value
LF data	$M_L = P_L = 21^2, x, y \in [.02, .98]$
HF data	$M_H = P_H = 6^2, x, y \in [.05, .95]$
Number of datasets	$N_L = N_H = 20$ values of a
λ_1	1
λ_2	1
λ_3	1×10^{-3}
λ_4	1×10^{-4}
SF learning rate	(1e-3, 5000, 0.9)
MF learning rate	(1e-3, 5000, 0.97)
SF network size	3 layers, 40 neurons
MF low-fidelity network size	3 layers, 30 neurons
MF linear network size	1 layer, 5 neurons
MF nonlinear network size	2 layers, 20 neurons

Table 6: Training parameters for the two-dimensional problem with nonlinear correlation.

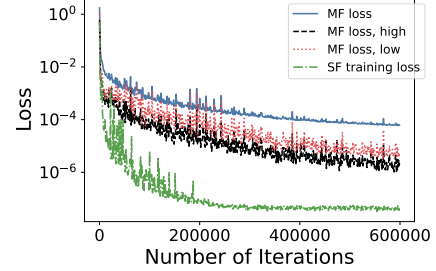


Figure 19: Training loss for the two-dimensional problem with nonlinear correlation.

B.5 Multiresolution ice-sheet modeling

Parameter	Value
LF data	$M_L = P_L = 2 \cdot 15^2$
HF data	$M_H = P_H = 2 \cdot 41^2$
MF datasets	$N_L = 100, N_H = 10$
SF datasets	$N_H = 10$ or $N_H = 50$
λ_1	1
λ_2	1
λ_3	1×10^{-3}
λ_4	1×10^{-4}
SF learning rate	(1e-4, 5000, 0.9)
MF learning rate	(1e-3, 5000, 0.97)
SF network size	3 layers, 200 neurons
MF low-fidelity network size	3 layers, 100 neurons
MF linear network size	1 layer, 10 neurons
MF nonlinear network size	2 layers, 100 neurons
Activation function	tanh or <code>relu</code> in JAX

Table 7: Training parameters for the multiresolution ice-sheet problem.

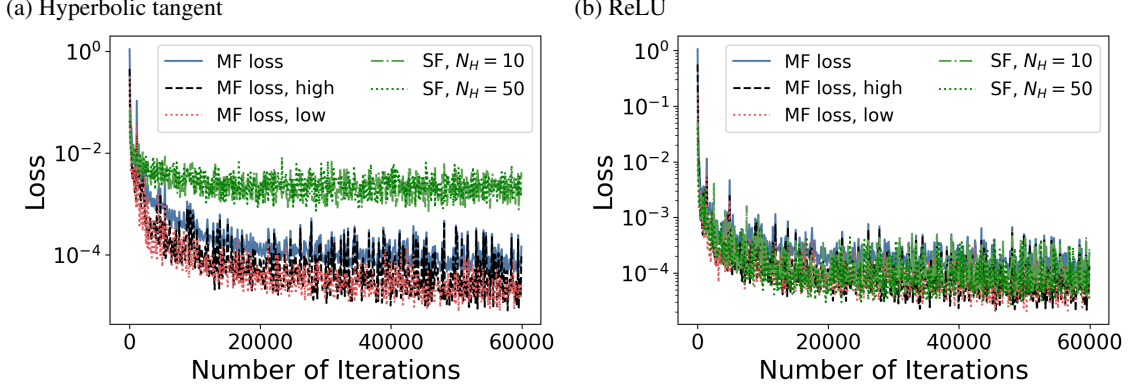


Figure 20: Training loss for the multiresolution ice-sheet problem with (a) hyperbolic tangent and (b) ReLU activation functions.

Method	Computational cost (hours)
Single fidelity, $N_H = 10$, tanh	1.40
Single fidelity, $N_H = 50$, tanh	1.35
Single fidelity, $N_H = 10$, ReLU	1.41
Single fidelity, $N_H = 50$, ReLU	1.41
Multifidelity, $N_H = 10$, $N_L = 100$, tanh	1.07
Multifidelity, $N_H = 10$, $N_L = 100$, ReLU	1.05

Table 8: Computational cost for the multiresolution ice-sheet problem (hours). For the single fidelity training the batch size is 10 values of u and for the multifidelity training the batch size is 5 values of u for both the low- and high- fidelity data. Reported times are on one NVIDIA P100 GPU.

B.6 Multiorder ice sheet modeling

Parameter	Value
LF data	$M_L = P_L = 2 \cdot 1426$
HF data	$M_H = P_H = 2 \cdot 1426$
MF datasets	$N_L = 80$, $N_H = 20$
SF datasets	$N_H = 20$
λ_1	1
λ_2	1
λ_3	1×10^{-3}
λ_4	1×10^{-4}
SF learning rate	(5e-5, 5000, 0.9)
MF learning rate	(5e-4, 5000, 0.97)
SF network size	4 layers, 150 neurons
MF low-fidelity network size	4 layers, 150 neurons
MF linear network size	1 layer, 10 neurons
MF nonlinear network size	3 layers, 150 neurons
Activation function	tanh in JAX

Table 9: Training parameters for the multiorder ice-sheet problem.

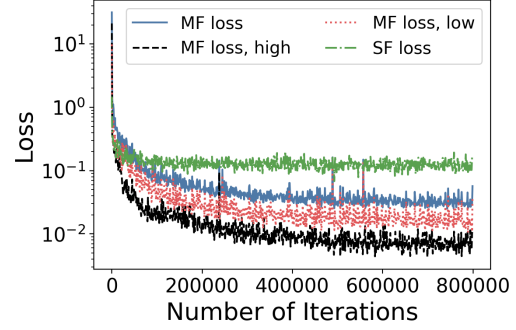


Figure 21: Training loss for the multiorder ice-sheet example.

Method	Computational cost (hours)
Single fidelity	2.68
Multifidelity	10.32

Table 10: Computational cost for the multiorder ice-sheet example (hours). For the single fidelity training the batch size is 20 values of u and for the multifidelity training the batch size is 20 values of u for both the low- and high- fidelity data. Reported times are on one NVIDIA P100 GPU.

B.7 One-dimensional physics-informed

Parameter	Value
LF data	$M_L = P_L = 21$
HF BC	$P_{BC} = 1$ at $x = 0$
HF collocation points	$P_p = 101$
Number of HF datasets	$N_H = 10$ values of a
Number of LF datasets	$N_L = 20$ values of a
λ_1	1×10^{-1}
λ_2	1
λ_3	1×10^{-2}
λ_4	1×10^{-4}
λ_5	0
λ_6	1×10^{-2}
SF learning rate	(1e-3, 2000, 0.9)
MF learning rate	(1e-3, 5000, 0.95)
SF network size	3 layers, 20 neurons
MF low-fidelity network size	3 layers, 30 neurons
MF linear network size	1 layer, 5 neurons
MF nonlinear network size	2 layers, 20 neurons

Table 11: Parameters for the one-dimensional physics-informed problem

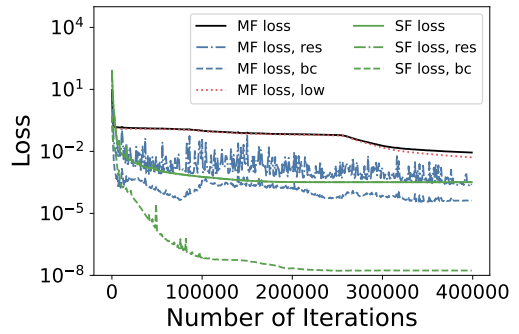
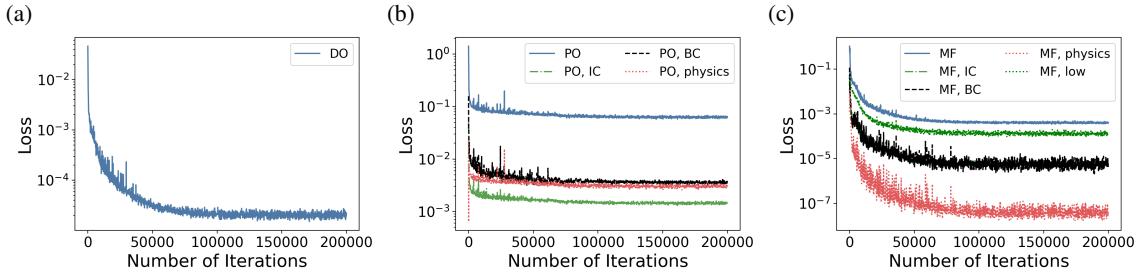


Figure 22: Training loss for the one-dimensional physics-informed problem.

B.8 Two-dimensional physics-informed (Viscous Burgers equation)

Parameter	Value
LF data	$M_L = 21, P_L = 21^2$
HF BC	$P_{BC} = 100$ at $x = 0$ and $x = 1$
HF IC	$P_{IC} = 101$ at $t = 0$
HF collocation points	$P_p = 2500$
Number of HF datasets	$N_H = 1000$
Number of LF datasets	$N_L = 1000$ or 200
λ_1	10
λ_2	1
λ_3	1×10^{-6}
λ_4	1×10^{-6}
λ_5	20
λ_6	1
DO learning rate	(1e-3, 2000, 0.9)
PO learning rate	(1e-3, 2000, 0.9)
MF learning rate	(1e-3, 2000, 0.9)
DO network size	7 layers, 100 neurons
PO network size	7 layers, 100 neurons
MF low-fidelity network size	7 layers, 100 neurons
MF linear network size	1 layer, 10 neurons
MF nonlinear network size	4 layers, 100 neurons

Table 12: Parameters for the viscous Burgers equation

Figure 23: Example of training loss for Burgers equation with $\nu = 10^{-4}$, $N_L = 1000$, and non-noisy data. (a) Data-only losses. (b) Physics-only losses. (c) Multifidelity losses.

Parameters	$\nu = 10^{-2}$ $N_L = 1000$	$\nu = 10^{-3}$ $N_L = 1000$	$\nu = 10^{-4}$ $N_L = 1000$	$\nu = 10^{-4}$ $N_L = 200$
Data-only	0.995	0.995	0.994	0.994
Data-only with noise	0.995	0.994	0.996	0.994
Physics-only	9.92	9.96	9.88	—
Multifidelity	14.26	14.46	14.21	14.21
Multifidelity with noise	14.55	14.19	14.56	14.25

Table 13: Physics-informed multifidelity: viscous Burgers equation. Computational cost for each case (hours). For the physics-only and multifidelity training, $N_H = 1000$. The high-fidelity batch size is 25 values of u and the low-fidelity batch size is 100 values of u . Reported times are on one NVIDIA P100 GPU.

C Non-composite Multifidelity DeepONets

In this section we consider the case where we have access to the low-fidelity data at every point in the high-fidelity training set and any location where we wish to output the operator values, as may be true if we know the exact function

that generates the low-fidelity data. We call this the “non-composite” framework, and refer to setup in the main text as the “composite” framework. The non-composite setup is shown in Fig. 24. We assume that we have high-fidelity data as described in Sec. 1.2.1. We also have a low-fidelity operator $y_L(u)(x)$ that we can use to generate values on the high-fidelity data points for input into the linear and nonlinear branch networks.

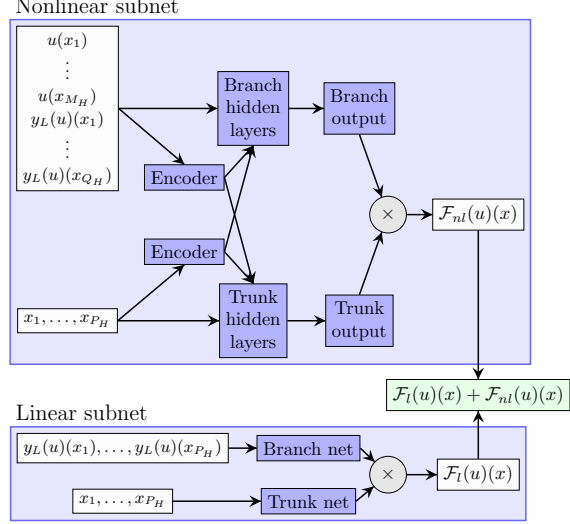


Figure 24: Non-composite multifidelity DeepONet setup.

We simultaneously train two DeepONets to learn the linear and nonlinear correlations between the low-fidelity operator and the high-fidelity operator. The loss function is given by

$$\mathcal{L}_{non-composite}(\theta) = \lambda_1 \mathcal{L}_{HF}(\theta_{nl}, \theta_l) + \lambda_3 \left(\sum w_{nl}^2 + \sum b_{nl}^2 \right). \quad (42)$$

We illustrate the impact of including an exact solver for the low-fidelity data instead of a DeepONet by considering the same example problem for both cases. We take

$$y_L(u)(x) = \sin(u) + x - 5.5 \quad (43)$$

$$y_H(u)(x) = \sin(u) \quad (44)$$

$$u = ax - 4 \quad (45)$$

for $x \in [0, 1]$ and $a \in [10, 14]$. Note that $y_H(u)(x) = y_L(u)(x) - x + 5.5$. The training parameters for the composite training are given in Tab. 14, results are given in Fig. 25b. The learned linear correlation is:

$$\mathcal{F}_l(u)(x) = 0.9998\mathcal{F}_{LF}(u)(x) - 0.9989x + 5.4989 - 0.00028x\mathcal{F}_{LF}(u)(x). \quad (46)$$

The training parameters for the non-composite training are given in 15, and the results are given in Fig. 25a. For this problem, we can recover the learned linear correlation as:

$$\mathcal{F}_l(u)(x) = 1.0000003y_L(u)(x) - 1.000002x + 5.500004 - 4.0047 \times 10^{-7}xy_L(u)(x). \quad (47)$$

Because the non-composite framework does not introduce errors from the low-fidelity DeepONet output, Eq. 47 is more accurate than Eq. 46, although both agree well with the exact equation.

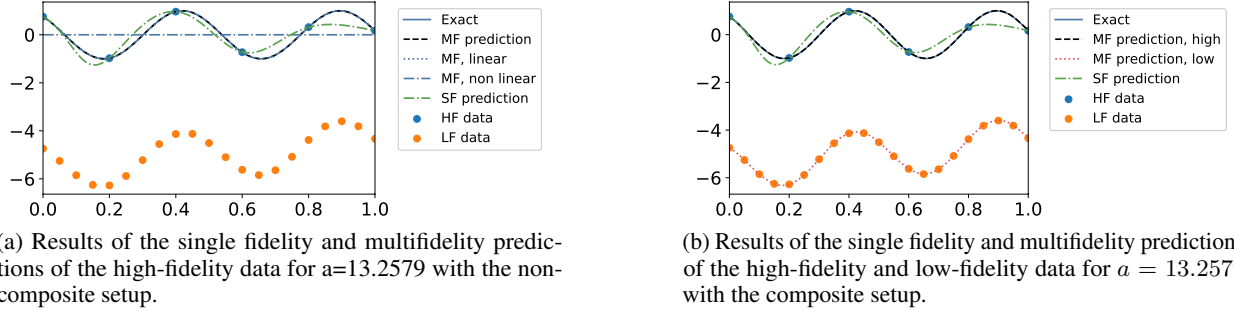


Figure 25: Comparison between the non-composite (a) and composite (b) setups.

Parameter	Value
LF data	$M_L = P_L = 21$
HF data	$M_H = P_H = 6$
Number of datasets	$N_L = N_H = 5$ values of a
λ_1	1×10^{-1}
λ_2	1
λ_3	1×10^{-1}
λ_4	1×10^{-3}
SF learning rate	(5e-3, 2000, 0.9)
MF learning rate	(1e-3, 5000, 0.97)
SF network size	3 layers, 30 neurons
MF low-fidelity network size	3 layers, 30 neurons
MF linear network size	1 layer, 5 neurons
MF nonlinear network size	2 layers, 20 neurons

Table 14: Parameters for the composite case.

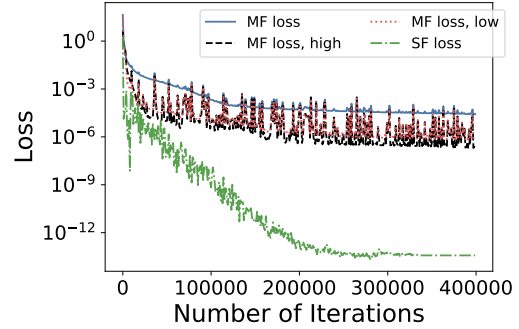


Figure 26: Composite loss.

Parameter	Value
LF data	$P_L = 21$
HF data	$M_H = P_H = 6$
Number of datasets	$N_H = 5$ values of a
λ_1	1×10^{-1}
λ_3	1×10^{-1}
SF learning rate	(5e-3, 2000, 0.9)
MF learning rate	(5e-5, 5000, 0.9)
SF network size	3 layers, 30 neurons
MF linear network size	1 layer, 7 neurons
MF nonlinear network size	2 layers, 20 neurons

Table 15: Parameters for the non-composite case.

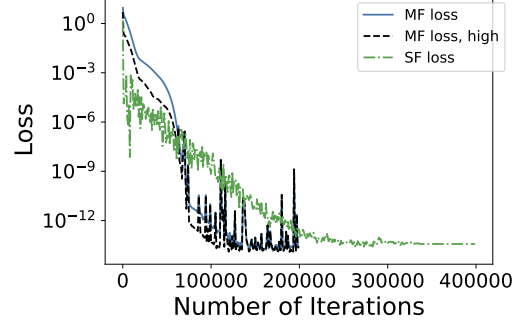


Figure 27: Non-composite loss.

D Mathematical models for ice sheets

We consider an ice sheet with domain $\Sigma \in \mathbb{R}^2$ that is fixed in time (the ice sheet can change thickness, but its domain does not change.) Denote the spacial coordinates by $(x, y, z) \in \mathbb{R}^3$, where $z = 0$ corresponds to sea level. The ice domain at time t is given by:

$$\Omega(t) := \{(x, y, z) \text{ s.t. } (x, y) \in \Sigma, \text{ and } l(x, y, t) < z < s(x, y, t)\},$$

where $\Gamma_l(t) := \{(x, y, z) \text{ s.t. } z = l(x, y, t)\}$ denotes the lower surface of the ice at time t and $\Gamma_s(t) := \{(x, y, z) \text{ s.t. } z = s(x, y, t)\}$ denotes the upper surface of the ice. The ice bed topography is assumed to be constant in time and is given by $\Gamma_b := \{(x, y, z) \text{ s.t. } z = b(x, y)\}$. Denote the ice velocity by $\mathbf{u} = (u, w, v)$.

D.1 Ice-sheet flow model

Many methods can be used to model the evolution of the ice sheet over time. At the highest order, land ice can be modeled as a shear-thinning Stokes flow driven by gravity.

The Stokes equation gives:

$$-\nabla \cdot \sigma = \rho g \quad (48)$$

$$\nabla \cdot \mathbf{u} = 0 \quad (49)$$

with pressure p , ice density ρ , stress tensor $\sigma = 2\mu\mathbf{D} - pI$, and strain rate tensor $\mathbf{D}_{ij}(\mathbf{u}) = \frac{1}{2} \left(\frac{\partial u_i}{\partial x_j} + \frac{\partial u_j}{\partial x_i} \right)$. The nonlinear viscosity is given by

$$\mu = \frac{1}{2} A(T)^{-\frac{1}{n}} D_e(\mathbf{u})^{\frac{1}{n}-1} \quad (50)$$

with $n \geq 1$, typically $n = 3$. A is the ice flow factor that depends on the ice temperature T . The *effective strain rate* $D_e(\mathbf{u}) = \frac{1}{\sqrt{2}} \|\mathbf{D}(\mathbf{u})\|$, where $|\cdot|$ denotes the Frobenius norm. Stokes equations are closed by the following boundary conditions:

$$\begin{cases} \sigma \mathbf{n} = 0 & \text{on } \Gamma_s \quad \text{stress free, atmospheric pressure neglected} \\ \sigma \mathbf{n} = \rho_w g \min(z, 0) \mathbf{n} & \text{on } \Gamma_m \quad \text{boundary condition at the ice margin} \\ \mathbf{u} = \mathbf{u}_d & \text{on } \Gamma_d \quad \text{Dirichlet condition at internal boundary} \\ \mathbf{u} \cdot \mathbf{n} = 0, (\sigma \mathbf{n})_{\parallel} = \beta \mathbf{u}_{\parallel} & \text{on } \Gamma_g \quad \text{impenetrability + sliding condition} \\ \sigma \mathbf{n} = \rho_w g z \mathbf{n} & \text{on } \Gamma_f \quad \text{back pressure from ocean under ice shelves} \end{cases}$$

$\beta(x, y)$ is the friction (or sliding) coefficient, which is typically difficult to measure and unknown and ρ_w is the density of the ocean water. The boundary condition at the margin includes the ocean back-pressure term, when the margin is partially submerged ($z < 0$).

The thickness of the ice is given by $H(x, y, t) = s(x, y, t) - l(x, y, t)$ on $\Sigma \times [0, t_f]$ and evolves according to

$$\partial_t H + \nabla \cdot (\bar{\mathbf{u}} H) = f_H \quad (51)$$

where $\bar{\mathbf{u}} := \frac{1}{H} \int_l^s \mathbf{u} dz$ is the depth-averaged velocity and f_H is an accumulation rate, accounting for accumulation and melting at the upper surface and at the base of the ice sheet. Typically, the ice margin is an outlet ($\bar{\mathbf{u}} \cdot \mathbf{n} > 0$) so no boundary condition are needed. We constrain H to be non-negative.

Because the Stokes equations are difficult and computationally intensive to solve, a series of simplified models have been derived. These models exploit the shallow nature of ice sheets to introduce approximations that decrease the computational intensity. We now introduce the Mono-layer higher-order (MOLHO) and Shallow Shelf Approximation (SSA) models.

D.2 Mono-layer higher-order (MOLHO)

MOLHO [13] model is based on the Blatter-Pattyn [e.g., 15] approximation that can be derived neglecting the terms w_x and w_y in the strain-rate tensor D and, using the continuity equation, replacing w_z with $-(u_x + v_y)$:

$$\mathbf{D} = \begin{bmatrix} u_x & \frac{1}{2}(u_y + v_x) & \frac{1}{2}u_z \\ \frac{1}{2}(u_y + v_x) & v_y & \frac{1}{2}u_z \\ \frac{1}{2}u_z & \frac{1}{2}v_z & -(u_x + v_y) \end{bmatrix}. \quad (52)$$

This leads to the following elliptic equations in the horizontal velocity (u, v)

$$-\nabla \cdot (2\mu \hat{\mathbf{D}}) = -\rho g \nabla s \quad (53)$$

with

$$\hat{\mathbf{D}} = \begin{bmatrix} 2u_x + v_y & \frac{1}{2}(u_y + v_x) & \frac{1}{2}u_z \\ \frac{1}{2}(u_y + v_x) & u_x + 2v_y & \frac{1}{2}v_z \end{bmatrix} \quad (54)$$

Here the gradient is two-dimensional: $\nabla = [\partial_x, \partial_y]^T$. The viscosity μ is given by (50) with the effective strain rate

$$D_e = \sqrt{u_x^2 + v_y^2 + u_x v_y + \frac{1}{4}(u_y + v_x)^2 + \frac{1}{4}u_z^2 + \frac{1}{4}v_z^2}.$$

The boundary conditions reads

$$\left\{ \begin{array}{ll} 2\mu\hat{\mathbf{D}}\mathbf{n} = 0 & \text{on } \Gamma_s \quad \text{stress free, atmospheric pressure neglected} \\ 2\mu\hat{\mathbf{D}}\mathbf{n} = \psi\mathbf{n} & \text{on } \Gamma_m \quad \text{boundary condition at ice margin} \\ \mathbf{u} = \mathbf{u}_d & \text{on } \Gamma_d \quad \text{Dirichlet condition at internal boundary} \\ 2\mu\hat{\mathbf{D}}\mathbf{n} = \beta\mathbf{u}_{||} & \text{on } \Gamma_g \quad \text{sliding condition} \\ 2\mu\hat{\mathbf{D}}\mathbf{n} = 0 & \text{on } \Gamma_f \quad \text{free slip under ice shelves} \end{array} \right.$$

where $\psi = \rho g(s-z)\mathbf{n} + \rho_w g \min(z, 0)\mathbf{n}$, which can be approximated with its depth-averaged value $\bar{\psi} = \frac{1}{2}gH(\rho - r^2\rho_w)$, r being the the submerged ratio $r = \max(1 - \frac{s}{H}, 0)$.

MOLHO model consists in solving the weak form of the Blatter-Pattyn model, with the ansatz that the velocity can be expressed as :

$$\mathbf{u}(x, y, z) = \mathbf{u}_b(x, y) + \mathbf{u}_v(x, y) \left(1 - \left(\frac{s-z}{H} \right)^{n+1} \right)$$

The problem is then formulated as a system of two 2d PDEs in \mathbf{u}_b and \mathbf{u}_v (for a detailed derivation see [13]). Note that the depth-averaged velocity is given by $\bar{\mathbf{u}} = \mathbf{u}_b + \frac{(n+1)}{(n+2)} \mathbf{u}_v$.

D.3 Shallow Shelf Approximation (SSA)

The shallow shelf approximation [30] is a simplification of the Blatter-Pattyn model, assuming that the velocity is uniform in z , so $\mathbf{u} = \bar{\mathbf{u}}$. It follows that $u_z = 0$ and $v_z = 0$, giving:

$$\mathbf{D} = \begin{bmatrix} u_x & \frac{1}{2}(u_y + v_x) & 0 \\ \frac{1}{2}(u_y + v_x) & v_y & 0 \\ 0 & 0 & -(u_x + v_y) \end{bmatrix}, \quad \hat{\mathbf{D}} = \begin{bmatrix} 2u_x + v_y & \frac{1}{2}(u_y + v_x) & 0 \\ \frac{1}{2}(u_y + v_x) & u_x + 2v_y & 0 \end{bmatrix}, \quad (55)$$

and $D_e = \sqrt{u_x^2 + v_y^2 + u_x v_y + \frac{1}{4}(u_y + v_x)^2}$. The problem simplifies to a 2D equation in Σ

$$-\nabla \cdot (2\mu H \hat{\mathbf{D}}(\bar{\mathbf{u}})) + \beta \bar{\mathbf{u}} = -\rho g H \nabla s, \quad \text{in } \Sigma$$

with $\bar{\mu} = \frac{1}{2}\bar{A}(T)^{-\frac{1}{n}} D_e(\bar{\mathbf{u}})^{\frac{1}{n}-1}$, where \bar{A} is the depth-averaged flow factor and with boundary conditions:

$$\left\{ \begin{array}{ll} 2\mu\hat{\mathbf{D}}(\bar{\mathbf{u}})\mathbf{n} = \bar{\psi}\mathbf{n} & \text{on } \Gamma_m \quad \text{boundary condition at ice margin} \\ \bar{\mathbf{u}} = \bar{\mathbf{u}}_d & \text{on } \Gamma_d \quad \text{Dirichlet condition at internal boundary} \end{array} \right.$$

Recall that $\bar{\psi} = \frac{1}{2}gH(\rho - r^2\rho_w)$, r being the the submerged ratio $r = \max(1 - \frac{s}{H}, 0)$. With abuse of notation, here Γ_m and Γ_d are intended to be subsets of $\partial\Sigma$.